RESEARCH PAPER

Experimental and Numerical Analysis of Aluminum-Polyethylene Composite Structure Subjected to Tension and Perforation Under Dynamic Loading for a Wide Range of Temperatures

A. Bendarma[1,2] · T. Jankowiak[2] · A. Rusinek[3] · T. Lodygowski[2] · C. Czarnota[3] · R. Bernier[3] · M. Khalfaoui[4]

Abstract

The aim of this work consists of identifying the material behavior of Alucobond composite structures subjected to ballistic impact. The composite is made of Aluminum alloy AW5005 and LDPE (low-density polyethylene). The mechanical properties of these materials are described in term of strain rate and temperature dependencies. Quasi-static tensile and compression tests for Alucobond are performed at four different strain rates, i.e. 0.0001 0.001, 0.01, and 0.03 s^{-1}. Moreover, in dynamic regime the used strain rate ranges in compression and perforation tests are ($10^4 \ s^{-1} \leq \dot{\varepsilon} \leq 10^5 \ s^{-1}$) at temperatures ranging from room temperature 20 °C to 100 °C. Various parameters influence the behavior of the Alucobond structure under impact: the geometry and the mechanical properties of the projectile, the initial impact velocity, and the thermomechanical behavior of the target. Numerous quasi-static and dynamic original test results (traction and perforation over a wide range of strain rates at room temperature and high temperature) are presented. Numerical simulations, particularly using the finite element (FE) method with the ABAQUS explicit code, are also effective supplements for theoretical and more detailed experimental investigations, which were carried out to analyze the dynamic behavior of impacted structures.

Introduction

Composite sandwich structures are a type of composite material that consists of two thin and stiff face sheets bonded to a lightweight and thick core material [1]. Sandwich structures are known for their high stiffness and strength-to-weight ratio, which make them ideal for various applications, such as aerospace, automotive, and marine industries [2].

The properties of composite sandwich structures depend on the type of materials used for the face sheets and core, as well as the thickness and arrangement of the layers [2]. The core material is typically made of foam or honeycomb structures, while the face sheets can be made of various fiber-reinforced composite materials, such as carbon, glass, or aramid fibers [2].

The dynamic behavior of composite sandwich structures is an important aspect that needs to be considered in their design and optimization for various applications. Under dynamic loading conditions, such as impact and vibration, the sandwich structures exhibit complex deformation and failure mechanisms, which can lead to reduced performance and even catastrophic failure [3]. Several factors affect the dynamic behavior of composite sandwich structures, including the type of core material, the thickness and properties of the face sheets, and the loading conditions [4]. The properties of the core material play a crucial role in the energy absorption capacity and damping behavior of the sandwich

✉ A. Bendarma
   b.amine@e-polytechnique.ma

1   Laboratory for Sustainable Innovation and Applied Research, Universiapolis, Technical University of Agadir, Bab Al Madina, Qr Tilila, BP 8143, 80000 Agadir, Morocco

2   Institute of Structural Analysis, Poznan University of Technology, Piotrowo 5, 60-965 Poznan, Poland

3   Laboratory of Microstructure Studies and Mechanics of Materials LEM3, University of Lorraine, 7 Rue Félix Savart, 57070 Metz, France

4   EST Salé, LASTIMI, Mohammed V University in Rabat, Salé, Morocco

structures [4]. For example, honeycomb core structures are known for their high specific energy absorption and good damping properties, while foam core structures exhibit better vibration damping and noise reduction properties [5].

Numerical modeling and experimental testing are commonly used to study the dynamic behavior of sandwich structures. Numerical modeling can provide insights into the underlying mechanisms of deformation and damage under dynamic loading conditions, while experimental testing can validate the numerical models and provide data for material characterization and model calibration [3]. Recent research focused on developing advanced materials and manufacturing techniques to enhance the dynamic performance of composite sandwich structures. For example, the addition of nanoparticles to the core material can improve the damping and energy absorption properties of sandwich structures [4]. Other approaches, such as the use of functionally graded materials and fiber-reinforced core structures, have been proposed to achieve tailored mechanical properties and enhanced performance under dynamic loading conditions [6]. However, composite sandwich structures are versatile and lightweight materials that offer excellent mechanical properties, but their dynamic behavior under various loading conditions needs to be carefully considered for safe and reliable operation in many applications. Further research is necessary to develop new materials and manufacturing techniques to improve the understanding of their dynamic behavior under different loading conditions. [7]

Polymers adopt a very different aspect and mechanical behavior depending on whether the temperature is below or above the glass transition temperature T_g.

- At low temperatures, the polymer is amorphous, rigid, and fragile, with Young's modulus of the order of 1000 MPa;
- Above the glass transition temperature, the mechanical behavior becomes viscoelastic, then rubbery with Young's modulus of the order of 1 MPa. The material can then undergo considerable hyperplastic elongations;
- At higher temperatures, the thermal agitation is such that the diffusion of the polymeric chains becomes very easy and the behavior is of a viscous fluid (this is the field of application of the shaping processes in the fused state).

The plastic behavior of amorphous polymers has been the subject of numerous experimental studies. For example, Bauwens [8–11] attempted to explain, from a microscopic point of view, the elementary mechanisms which control the plastic deformation of these polymers, and from a macroscopic point of view, the dependence of these materials on the various stress conditions. However, each study describes the behavior of the polymers using only one type of mechanical test, often the uniaxial tensile test. Although this test is

successful in obtaining large deformations, it is not suitable for studying the plasticity of polymers. The curves in Fig. 1, are obtained with the video metric method during a tensile test, corresponding to the behavior at large deformation for various amorphous and semi-crystalline polymers (PEEK, PA6, PC, PVC, PP, PE, PTFE) at ambient temperature.

Although there has been an extensive research on the mechanical properties of thermoplastic polymers, there is still a lack of understanding regarding the impact and perforation behavior of these polymers at different temperatures. Daniel et al. [14] work aims to analyze the influence of temperature and the associated polymeric transitions on the mechanical response of PMMA (Polymethyl Methacrylate) under high impact velocity. Testing temperatures ranging from 20 °C to 140 °C are covered in this comprehensive study. In order to gain insights into the deformation and failure mechanisms during the perforation process, a series of tests were conducted using uniaxial compression under both quasi-static and dynamic conditions at various initial temperatures. A new constitutive model is proposed to analyze the deformation mechanisms that govern the mechanical behavior of PMMA, particularly above the glass transition temperature [14]. This model considers finite deformations as well as dependencies on temperature and strain rate. Other polymers revealed strain rate and thermal sensitivities, for example, LDPE which is investigated in the present paper.

These material transitions are associated with the free volume and mobility of polymeric chains, which are closely linked to temperature and strain rate. At lower strain rates, the failure transition occurs at lower temperatures, which is why we chose to conduct tests at lower temperatures. Additionally, as the strain rate increases, the failure transition shifts to higher temperatures.

Based on the quasi-static results (Fig. 2a), a transition from pseudo-brittle to ductile behavior is observed at a
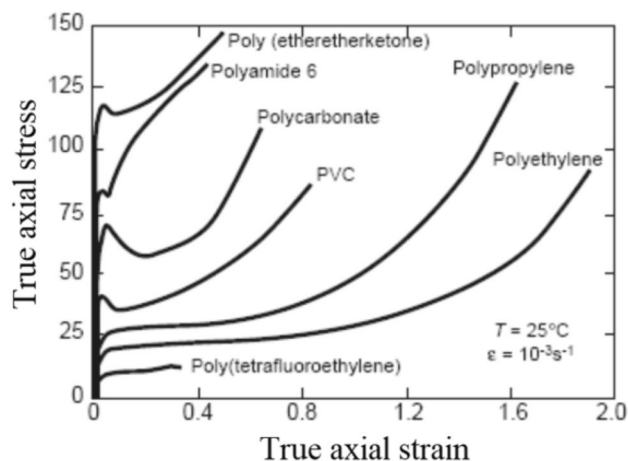

Fig. 1 True strain curves—true deformation of various polymers obtained at 25° C. [12, 13]
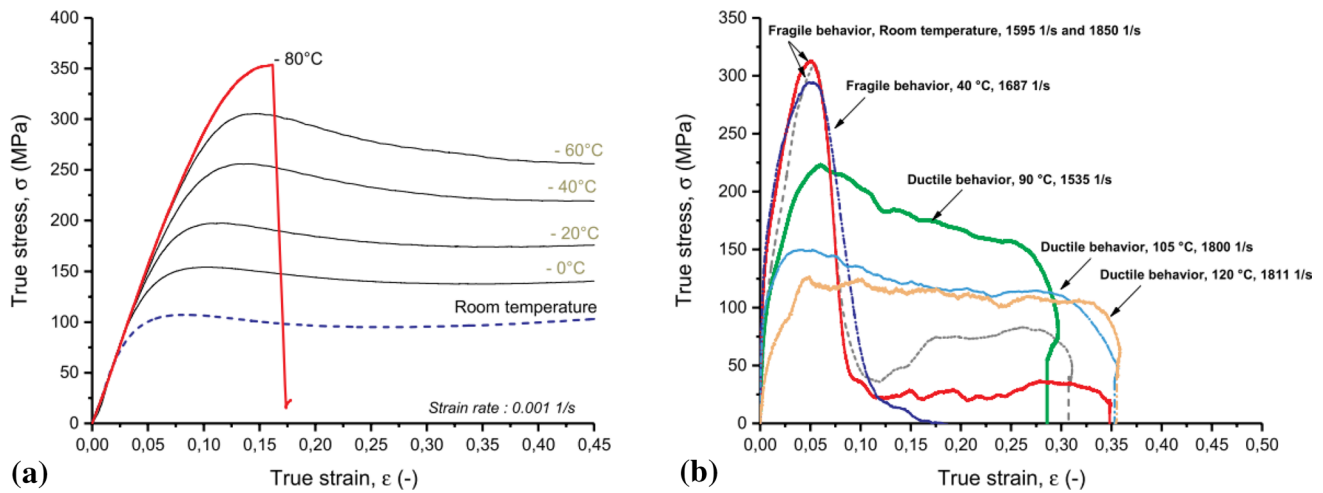
Fig. 2 Material behavior description: **a** Temperature effect under quasi-static loading; **b** Temperature effect under dynamic loading [14]

temperature threshold within the range of $60\,°C \leq T_0 \leq 80\,°C$. Above this threshold, a pseudo-brittle behavior is observed, with failure strain values around 15%. Furthermore, a decrease in temperature also leads to higher yield strength. For testing temperatures above this threshold, a ductile behavior is observed.

According to the dynamic results shown in Fig. 2b, a transition from pseudo-brittle to ductile behavior is observed at a temperature threshold of $T_0 = 40\,°C$ Above $T_0 = 40\,°C$, and the material starts exhibiting a ductile behavior. This shift in the brittle to ductile transition under dynamic loading, compared to quasi-static loading (see Fig. 2a), can be attributed to the interplay between temperature and strain rate effects on the mobility of polymeric chains. Increasing the temperature promotes chain mobility, leading to increased ductility, while higher strain rates hinder chain mobility. In the case of

dynamic loading, the material is observed to be brittle at low temperatures and room temperature (Fig. 2b) [14].

Further dynamic characterization was conducted at high temperatures, specifically $T_0 \geq Tg$ (glass transition temperature). The purpose of this analysis was to study the mechanical behavior of PMMA in the rubbery region, where a ductile response is expected. The hardening behavior was observed to change at temperatures higher than $T_0 \geq 120\,°C$, as shown in Fig. 3 for two strain rates. It is worth noting that two reference strain rates were used to facilitate the interpretation and comparison of the results presented in Fig. 3. This change in behavior can be attributed to the increased influence of the polymeric network on the overall stress response.

Based on these results, it can be concluded that the energy required to cause failure increases with temperature introducing a large ductility and is accompanied by a significant
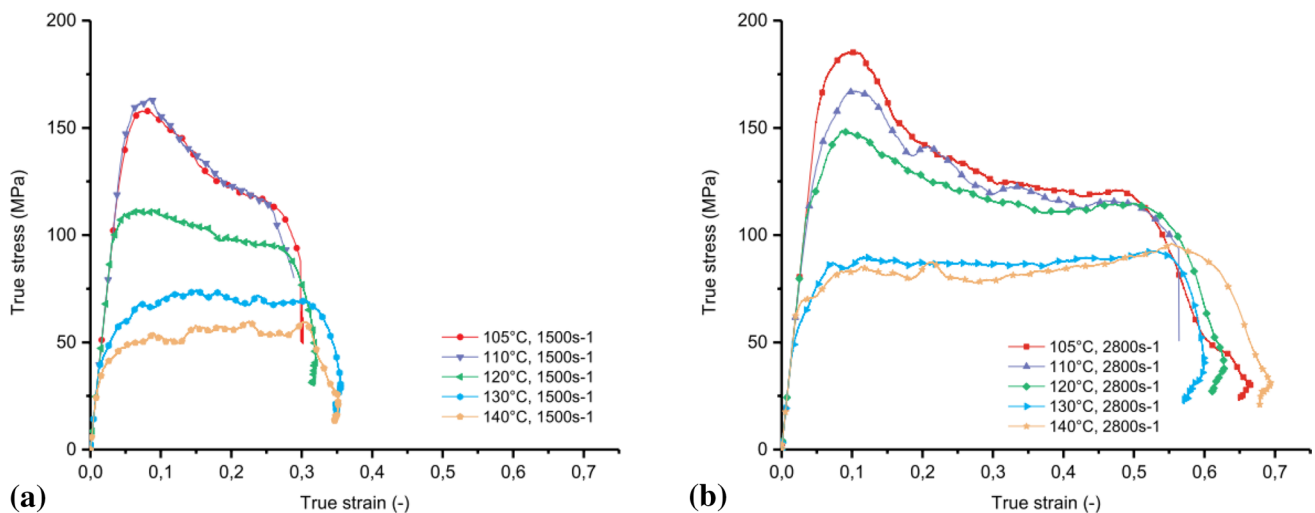

Fig. 3 Material behaviour of PMMA for different initial temperatures; **a** 1500 1/s; **b** 2800 1/s [14]

increase in ductility. This observation is crucial for analyzing the structural behavior under dynamic loading.

Arruda et al. [15] showed the influence of temperature on the mechanical behavior of polymers, especially for PMMA. The elastic limit (flow stress), Young's modulus, as well as hardening decreases as the temperature increases. The results show that the temperature has a significant influence on the elastic limit. This increase in the elastic limit at low temperatures is accompanied by a greater fragility, which limits the use of certain polymers in extreme conditions.

In fact, this sensitivity to temperature proves that the physical mechanisms governing the plastic deformation of polymers change according to the temperature ranges.

Recent research, exemplified by Jordan et al. [16] to understand the complex mechanical properties of low-density polyethylene (LDPE). The meticulous analysis by Jordan et al. systematically explores the response of LDPE to dynamic loading conditions, highlighting the complex interplay between strain rate and temperature dependence within this thermoplastic polymer.

The mechanical properties of polymers, in particular their dependencies on temperature and strain rate, are considered of paramount importance for their practical implementation in design. In this study, the compressive behavior of low-density polyethylene (LDPE) was examined over a range of strain rates and temperatures. The mechanical response of LDPE was found to be dependent on temperature and strain rate, with stress increasing as strain rate increased or temperature decreased. A consistent linear relationship was observed between flow stress, temperature, and the logarithm of strain rate over the entire range of conditions studied. Temperature and strain rate data were mapped. based on time–temperature superposition, using a single mapping parameter. This analysis suggests the absence of phase transitions over the entire range of velocities and temperatures studied. In addition, Taylor impact experiments were carried out, revealing a double zone of deformation and flow boundary measurements consistent with those obtained during compression experiments.

In their rigorous analysis, Jordan et al. [16] have revealed essential information about the behavior of LDPE at different strain rates and temperatures, establishing a comprehensive framework for interpreting the material's dynamic response. Their work forms the fundamental basis on which we are building our own research, using their fundamental findings to further investigate the behavior of LDPE.

LDPE shows both strain rate and thermal sensitivities. Figure 4 reports the dependence of the stress, at different levels of strains, in terms of temperature, for dynamic and static loading conditions. It is observed that the sensitivity of LDPE to temperature is twice as large at high strain rates.

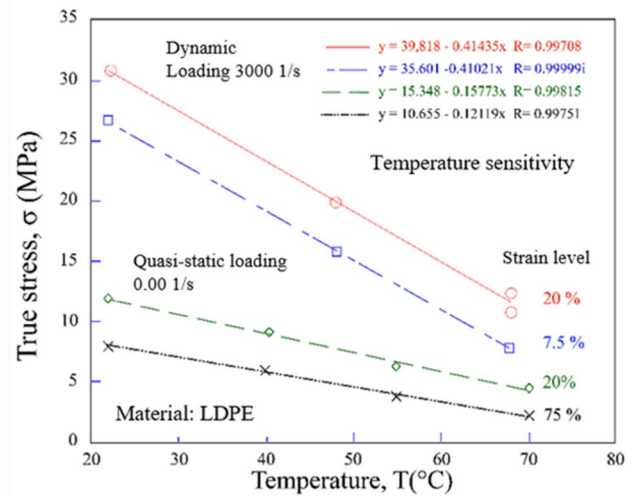Combining Fig. 4. with the strain rate dependence of LDPE at room temperature (results not reported here) and

Fig. 4 True stress versus temperature for a strain level of 7.5% and 20% under quasi-static and dynamic loading, [16]
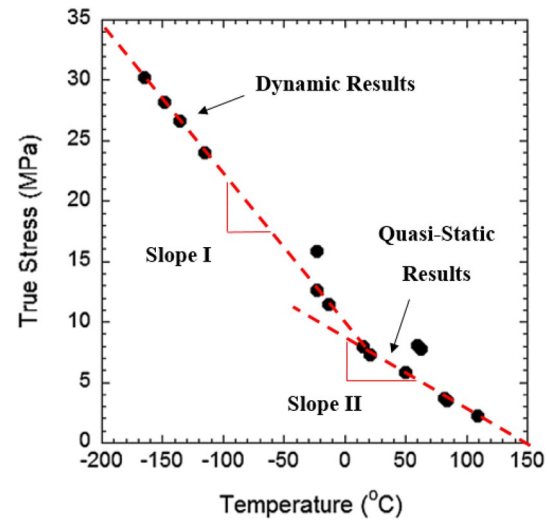

Fig. 5 True stress versus temperature at quasi-static and dynamic strain rates in LDPE, [16]

using the strain rate–temperature equivalence, Jordan et al. [16] proposed a mapping of true stress versus temperature, see Fig. 5. It is observed that the stress decreases with temperature, with a value close to zero when the melting temperature (≈ 115 °C) is reached. In Fig. 5, the mapped data shows good agreement with the data tested at the reference strain rate under various temperatures. However, there is a significant deviation observed in the data tested at high strain rates with varying temperatures. Notably, the slopes of the lines fitting the temperature-dependent data in Fig. 4 at low and high strain rates are not parallel, contrary to what would be expected if a single parameter were sufficient to map all the data [16].

Based on the results of Figs. 4 and 5, it is expected that during perforation tests at high temperatures, the polyethylene layer will degrade according to the temperature increase, and consequently may have an effect on the response of the ALUCOBOND composite structure Note that the polymer represents 80% by volume of the composite structure. Therefore, it is important to understand the effect of temperature on the plastic flow of the polymer as well as on the structure. For this reason, a perforation test device at high temperatures has been developed in order to validate experimental observations performed during characterization tests such as tension and compression. For quasi-static tests, the strain level was 7.5% and the strain rate was equal to $10^{-4}\ s^{-1}$. As in [16], the dynamic results were deduced from a mapping between temperature and strain rate using a single mapping parameter, A, based on the time–temperature superposition of polymers.

Metals under dynamic testing are subjected to high strain rates and short loading times, which can lead to unique material behavior and failure mechanisms [17]. Dynamic testing is an essential aspect of materials science and engineering as it helps to predict the behavior of metals under extreme conditions such as high-speed impacts, explosions, and ballistic events [18]. Understanding the mechanical response of metals under dynamic loading conditions is critical for improving the safety and reliability of structural components in various fields such as aerospace, defense, automotive, and industrial applications [19]. In recent years, experimental techniques for characterizing the dynamic behavior of metals have advanced significantly. High-speed cameras, laser interferometry, and other sophisticated measurement tools have enabled researchers to capture detailed information about the deformation and failure processes of metals under dynamic loading [20, 21]. Numerical simulations, such as finite element analysis, have also been used to model and predict the response of metals under dynamic conditions. [7, 22–32].

Bendarma et al. [33] investigated the dynamic behavior of aluminum alloy AW 5005 under high strain rates and temperatures. The study focused on the effect of interfacial friction and specimen configuration on the dynamic response of the material using a Split Hopkinson Pressure Bar (SHPB) system. The results showed that interfacial friction has a significant effect on the dynamic response of the material, with an increase in friction leading to a decrease of the peak stress and strain. The study also highlighted that the geometry of the specimen can affect the dynamic response of the material, with a thinner specimen showing higher strain rates and higher peak stresses than a thicker specimen. The findings of this study provide valuable insights into the behavior of aluminum alloy AW 5005 under dynamic loading conditions and can be used to inform the design of structures and components that are subjected to high strain rates and temperatures.

Overview of the Studied Materials

The aim of this study is to explore the potential use of a new composite material called ALUCOBOND [34] for constructing and protecting buildings, as for other civil engineering applications. This material is known for its rigidity, excellent resistance to weather and impact, ability to absorb vibrations, and ease of installation. ALUCOBOND is manufactured from a continuous rolling process with different core thicknesses, and can be customized according to specific size requirements [34].

In the present work, ALUCOBOND is a composite panel consisting of two aluminium cover sheets (each 0.5 mm thick) made of Peraluman-100 (also referred to as AlMg1 or EN AW-5005) and a mineral-filled polymer core (3 mm thick). (Fig. 6). The two constituents are described in the following sections.

Aluminum AW 5005 Description

The aluminum alloy AW5005 contains nominally 0.8% magnesium and presents a medium strength, good weldability,

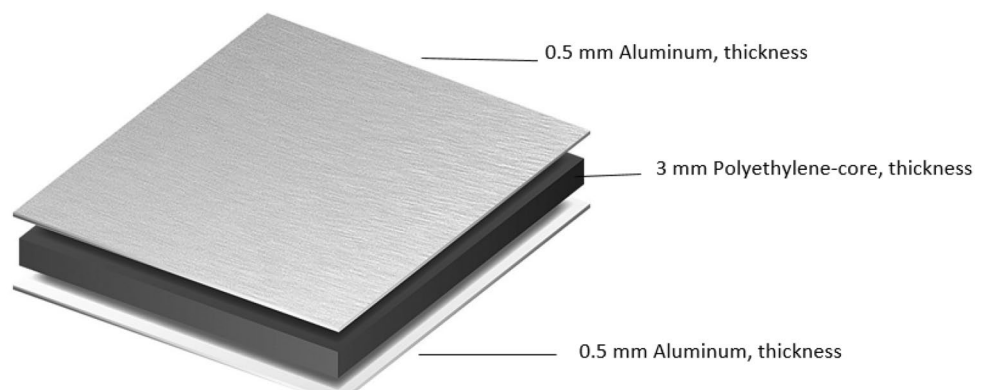**Fig. 6** Scheme of 3 layers used for the ALUCOBOND [34]

0.5 mm Aluminum, thickness

3 mm Polyethylene-core, thickness

0.5 mm Aluminum, thickness

Table 1 Chemical properties of the EN AW 5005 aluminum alloy [35]

Chemical Composition %	Fe	Si	Cu	Mn	Mg	Zn	Cr	Al
	0.45	0.3	0.05	0.15	0.5–1.1	0.2	0.1	Balance

Table 2 Mechanical properties of the EN AW 5005 aluminum alloy [35]

Mechanical properties	Yield Stress (MPa)	Tensile strength (MPa)	Elongation (%)	Hardness (HV)
	45	110	15	32

Table 3 Properties of low-density polyethylene [39]

Property	Value	Range/comments
Density, g/cc	0.91	0.910–0.925
Hardness, shore D	44	41–46
Tensile strength, yield MPa	10	4–16(ASTM D638)
Tensile strength, ultimate MPa	25	7–40
Modulus of elasticity, GPa	0.2	0.07–0.3; in tension (ASTM D638)
Flexural modulus, GPa	0.4	0 – 0.7: (ASTM D790)
Coefficient of linear thermal expansion at 20 °C, mm/(m °C)	30	20 – 40 mm/(m°C);(ASTM D696)
Melting point, °C	115	–

and corrosion resistance in marine atmospheres. The metallurgical state of the aluminum alloy used in this work is as received. It has a lower density and excellent thermal conductivity compared to other aluminum alloys. It is the most commonly used type of aluminum in sheet and plate forms [35–37]. The EN AW 5005 aluminum alloy has been investigated in our experimental results. The chemical composition is reported in Table 1 while some mechanical properties are shown in Table 2.

Low-Density Polyethylene Description

Low-density polyethylene (LDPE) is a thermoplastic originally prepared by high-pressure polymerization of ethylene. It was the first grade of polyethylene, produced in 1933 by Imperial Chemical Industries (ICI). Its comparatively low density arises from the presence of a small amount of branching in the chain (about 2% of the carbon atoms) [35] its manufacturer employs the same method today. Despite competition from more modern polymers, LDPE continues to be an important plastic grade.

LDPE is defined by a density range of 0.910–0.940 g/cm^3. It is not reactive at room temperatures, except by strong oxidizing agents, and some solvents cause swelling. It can withstand temperatures of 80 °C continuously and 95 °C for a short time. Made in translucent or opaque variations, it is quite flexible and tough [38] (Table 3).

Low-density polyethylene (LDPE) has been commonly used due to its versatile characteristics and usefulness. These traits facilitated the application of plastics to almost all industrial, agricultural, or domestic markets [39].
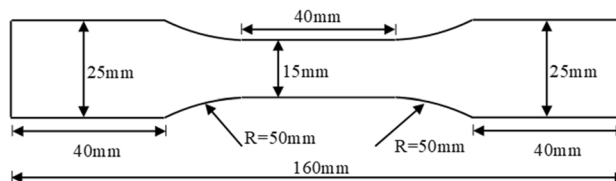
Experimental Conditions and Techniques

Tensile Test Description

The quasi-static tests of this work were carried out on an Instron universal traction machine of type 5585H equipped with a 10 KN load cell, an Instron AVE 2663-821 video

Fig. 7 Dimensions of the tensile specimens, [36, 41]

extensometer, a climatic enclosure regulated by a Eurotherm 2408 type controller (the manufacturer's site [40]). The test is controlled by a computer via the Bluehill modular software. A tensile loading, under constant loading rate, is applied to the specimen up to failure. The range of studied strain rates varies from 10^{-4} s^{-1} to $10^{-1}s^{-1}$. For material stresses greater than $10^{-1}s^{-1}$ at strain rate, the experimental means of dynamic loading has been used in traction. The plane geometry as well as the dimensions of the flat specimens used in this work (quasi-static tests) are presented in Fig. 7 [41]. Some specimens were machined from cold-rolled 1 mm aluminum sheets and other from an Alucobond structure with two 0.5 mm thick aluminum plates and a 3 mm thick polyethylene plate, see Fig. 6.

During the test the elongation of the specimen ΔL and tensile force F are measured. The nominal strain and stress are calculated using the following formulae:

$$\begin{cases} \sigma_n = \frac{F}{A_0} \\ \varepsilon_n = \frac{\Delta L}{L_0} \end{cases} \quad (1)$$

where A_0 is the initial cross-section of the specimen and L_0 its initial length. Under this assumption of volume

conservation, the true stress and strain in the specimen can be expressed as:

$$\begin{cases} \sigma = \sigma_n(1 + \varepsilon_n) \\ \varepsilon = ln(1 + \varepsilon_n) \end{cases} \qquad (2)$$

This formulation is valid only in the pre-necking domain.

Perforation Test Description

This section details the mechanical response of Alucobond sheets under impact loading. This perforation process has been thoroughly analyzed for steels and aluminum by combing experimental, analytical, and numerical investigations [36, 42]. Here, a similar approach is adopted to analyze the perforation tests in the composite structure. The tests encompassed a wide range of impact velocities spanning from 40 to 180 m/s, using a conical projectile with a diameter of 13 mm and an angle of 72° impacting a 4.0 mm thick plate structure, see Fig. 6. The active region of the specimen during perforation is defined in Fig. 8.

The projectile, of mass m_p, is launched using a pneumatic gas gun. It accelerates in the tube, Fig. 9, to reach the exit with the initial impact velocity denoted by V_0. Then, depending on the kinetic energy $\frac{m_p}{2} V_0^2$, involved in the process, and the properties of the sample material, the projectile may impact the aluminum sheet with a partial or a complete perforation. Sensors are used to measure the initial velocity V_0 and a laser barrier for the residual velocity of the projectile in case of complete perforation, Fig. 9.

The projectile, of mass $m_p = 28$ g, is made with heat-treated maraging steel to reach yield stress about 2 GPa [42]. The gas gun set-up is described in Fig. 9.

The gas gun (Fig. 9), has the following main characteristics:

- Launcher tube diameter: 13 mm.
- Launcher tube length: 5 m
- Impact speed range: 30 to 180 m.s^{-1} for a 28 g mass projectile.
- Power supply: Laboratory compressed air network with a maximum pressure of 10 bar.

The residual velocity of the projectile can be expressed using the equation of Ipson and Recht, [22, 43–45] Eq. 3. As mentioned a conical projectile shape has been used which induces that the mass of the plug is nil. The relationship used to calculate the residual velocity is given by:

$$V_R = \left(V_0^{\kappa} - V_B^{\kappa}\right)^{1/k} \qquad (3)$$

where V_0 is the initial velocity, V_B the ballistic velocity, and κ is the ballistic curve shape parameter.

The energy absorbed by the plate E_d can be calculated using the following equation:

$$E_d = \frac{m_P}{2}\left(V_0^2 - V_R^2\right) \qquad (4)$$

Experimental data are used to calculate the difference between initial and residual kinetic energy, and the Recht-Ipson approximation can be employed to determine the amount of energy absorbed by the plate. Note that Jones et al. [43, 44] and Grytten et al. [46], studying the impact and perforation of metal plates have shown that square and circular plates have similar ballistic properties, energy absorption capacity, and failure modes, provided that the side length of the square plate is equal to the diameter of the circular plate and all other parameters are identical. In other words, for sufficiently large specimens, the results are not depending on the boundary conditions.

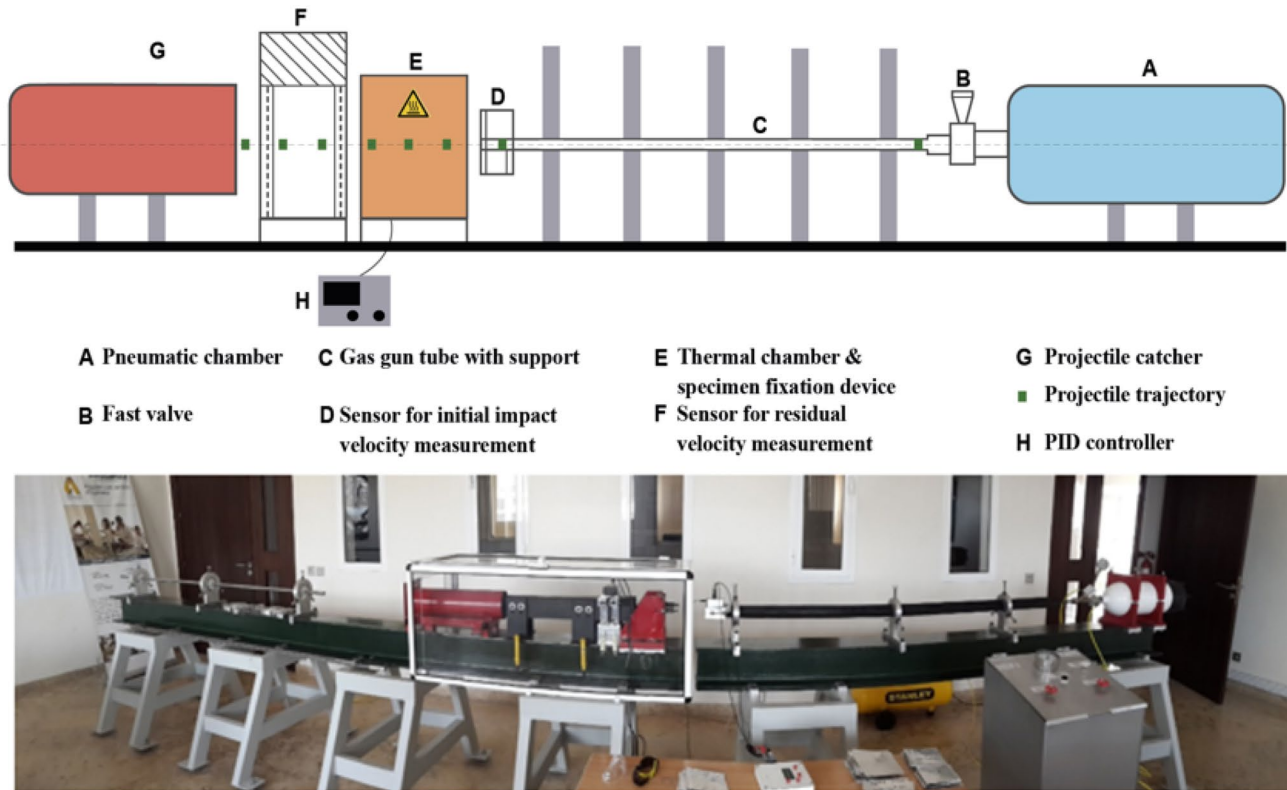**Fig. 8** Dimensions of the projectile and target used during perforation tests [36]

(a) Target

(b) Conical projectile
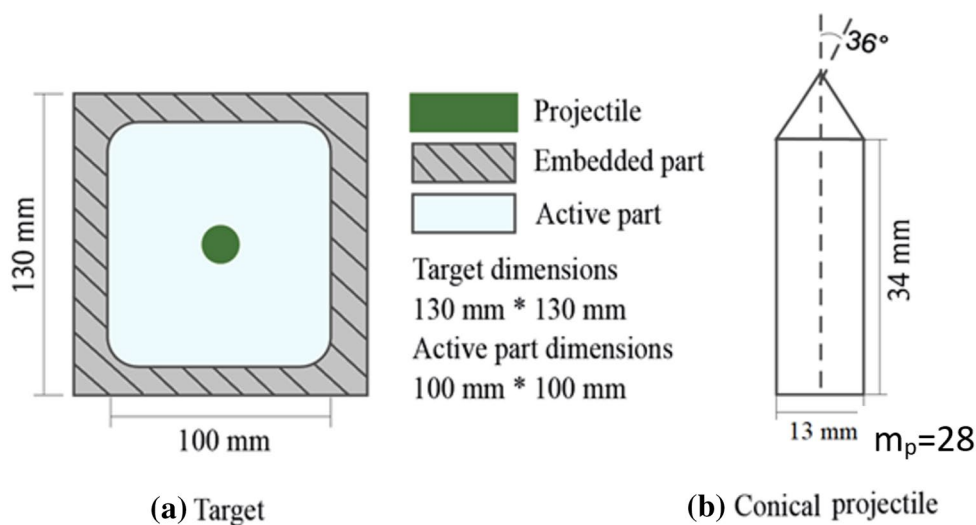
Fig. 9 Gas gun set-up used for perforation tests at high impact velocities and temperatures

Perforation Test Using a Thermal Chamber

A specific oven has been developed with a (maximum temperature of 300 °C) to test and analyze the ballistic response behavior of polymers at high temperatures (Patent Number MA41357A). This device has been used to test different polymers having a melting temperature close to 300 °C (e.g. as for example: Polyester, Nylon, Polycarbonate, and Polystyrene).

The principle of the heating system as well as the photo of the apparatus are shown in Fig. 10. The air flows inside the system using a ventilator. A sarcophagus is used around the plate specimen to have a uniform temperature distribution. Therefore, the two sides of the specimen are heated up at the same time.

A calibration step was implemented in order to control the heating process and ensure homogeneity of the resulting temperature. The temperature evolutions in the thermal chamber and in the specimen (captured by two thermocouples during the calibration process) are reported in Fig. 11. It has been verified that for tests at elevated temperature (above 50 °C), a time $t_{waiting} \approx 20min$ was sufficient to get uniform temperature distribution inside a steel specimen and a PMMA specimen, see Fig. 11.

In the present work, the composite layered structure of Fig. 6 has been tested with the perforation setup equipped with the thermal chamber at a temperature varying from 20 °C to 300 °C. The aim is to evaluate how the temperature and strain rate sensitivities of the constituents are transposed at the level of the composite structure.

Analysis and Discussion

Aluminum Alloy AW 5005 Characterization Results

Experimental Analysis of the Aluminum Alloy

This material has been characterized in a previous work [36]. This section is dedicated to recall the main obtained results. Aluminum 1 mm thick sheets were used to create test sample parts for tensile testing and to machine compression pellets. The outcomes will be categorized based on the type of stress applied (tension, compression, and perforation). There is limited literature available on this material, specifically regarding the mechanical properties of this particular aluminum alloy. Kulekci et al. [35], reported that a tensile yield shear strength of 45 MPa and a tensile shear strength
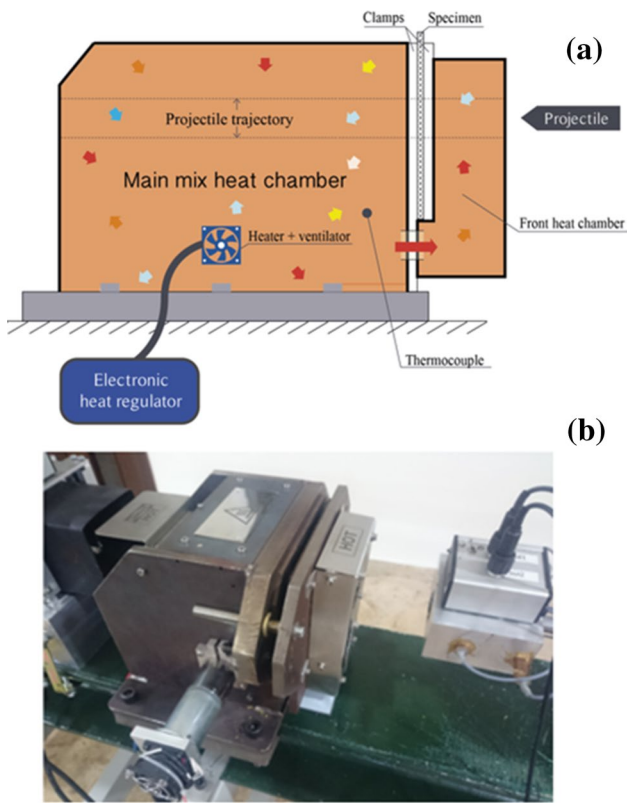
Fig. 10 Thermal chamber for heating up target plate specimens, **a** scheme **b** general view of the apparatus (Patent Number MA41357A)

of 110 MPa. Additionally, it was noted that the elongation of this alloy is approximately 15%. In this study, a tensile test is conducted to calibrate the material's behavior. Quasi-static tensile tests were conducted at four different strain rates: 0.001, 0.01, 0.1, and 0.15 s^{-1}. The resulting stress–strain curves are presented in Fig. 12. The experimental results demonstrate that the yield stress and strain hardening of the AW5005 aluminum alloy are almost not sensitive to strain rate in the slow loading rates regime explored here. However, the true strain values at failure, ranging from 0.042 to 0.1, are highly depending on the strain rate. It is observed that the ductility increases with the strain rate (see Fig. 12). The average yield strength of the AW5005 aluminum was found to be close to 147 MPa [36].

The study involved also experimental and analytical, investigations to analyze the perforation process [42]. A broad range of impact velocities from 40 to 180 m/s were tested. The projectile used had a 13 mm diameter and a 72° angle conical shape, while the plate was 1.0 mm thick. Figure 6 shows the active part of the specimen during perforation. The results in terms of the ballistic curve V_R-V_0 are presented in Fig. 13-a.

Experimental results have been used to identify parameters involved in Eq. (3) [43]. The constant V_B is equal to 40 m/s, and the ballistic curve shape parameter k is equal to 1.65. The absorbed energy by the plate, E_d, has been calculated using Eq. (4).

The difference between the initial and residual kinetic energy can be determined using experimental data. Based on the Recht-Ipson approximation, the energy absorbed by the
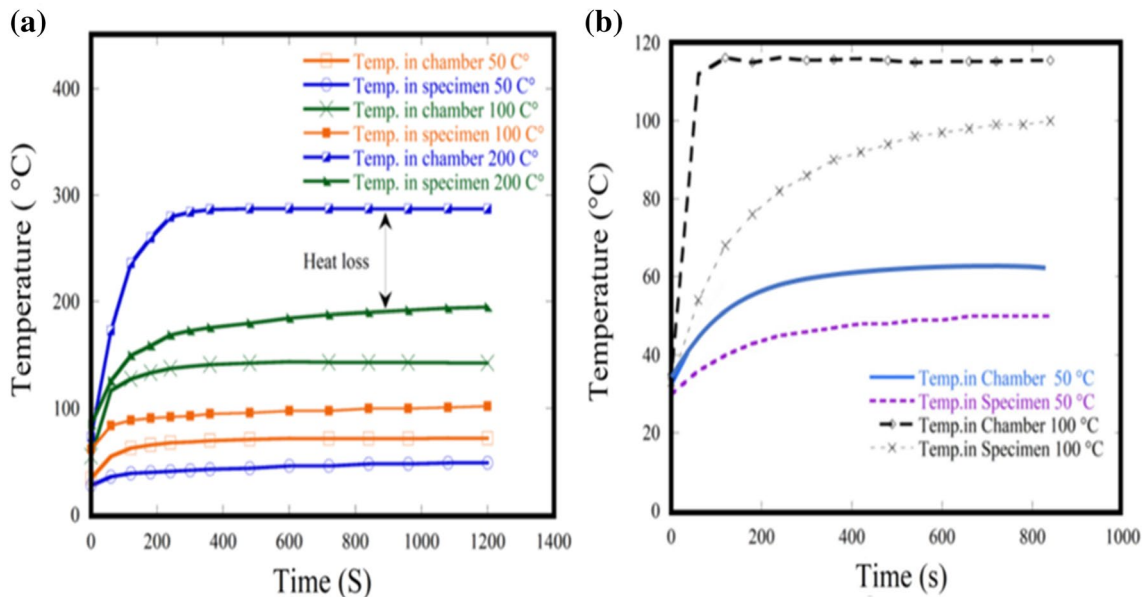

Fig. 11 Calibration of the system—thermocouples records inside the thermal chamber and on specimen surface for different imposed temperatures, **a** Metal: Steel, **b** Polymer: PMMA
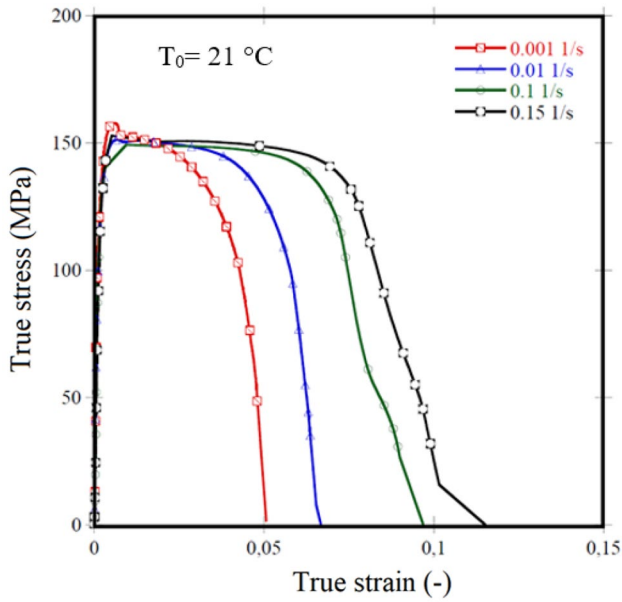
Fig. 12 Stress–strain curves for different strain rates at room temperature, aluminum AW5005 [36]

plate can then be calculated (see Fig. 13b). Using Eq. 4, the minimum energy required for perforation is 28 J ($m_P = 28g$ and $V_0 = V_B = 40m/s$).

Figure 14 shows the failure pattern for an initial impact velocity of $V_0 = 85$ m/s, with four petals and a residual velocity of $V_R = 66.5$m/s. The same failure pattern is observed for an initial impact velocity of $V_0 = 132.3$ m/s, with a residual velocity of $V_R = 120.2$m/s,. The number of petals is four for the entire range of impact velocities tested, from 40 to 180 m/s. A detailed discussion of the number of petals and how it depends on the projectile shape and failure mode can be found in [47].

In order to define completely the material behavior, a failure criterion has been proposed by Bendarma et al. [36] to combine with the Johnson–cook constitutive relation (Eq. 5) [48].

$$\sigma = \left(A + B\varepsilon_{pl}^n\right)\left(1 + Cln\frac{\dot{\varepsilon}^p}{\dot{\varepsilon}_0}\right)\left(1 - T^{*m}\right) \tag{5}$$

The material constants obtained from experimental tests are reported in Table 4 [33, 36].
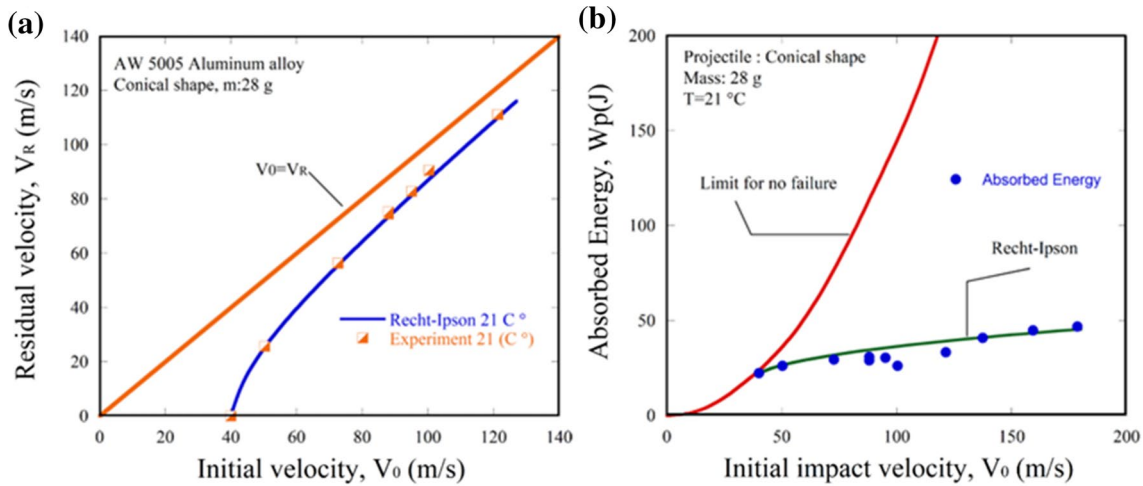
Fig. 13 **a** Ballistic curve obtained during perforation and determination of the ballistic limit, **b** Energy absorbed by the plate during impact test, determination of the failure energy [36]

Fig. 14 Experimental observation of failure patterns, $V_0 =$ 85.3 m/s and 132.3 m/s [36]

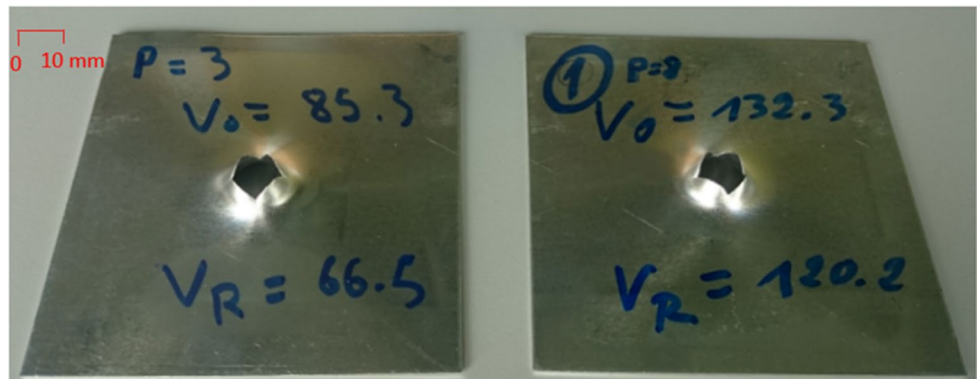**Table 4** All material parameters for Johnson–Cook model [31]

A (MPa)	B (MPa)	n (−)	C (−)	m (−)	T_m(K)	T_0(K)
147	60	0.9	0.003	1.08	933	300
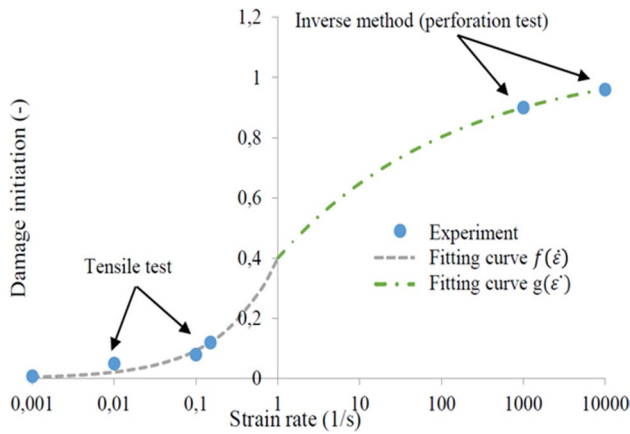
Fig. 15 Plot of failure strain versus plastic strain rate using optimized model. [36]

$$J = H_1 \dot{\varepsilon}_T^{\alpha_1} + H_2 \dot{\varepsilon}_T^{\alpha_2} \tag{7}$$

This model thus involves five independent parameters, see Table 6, from which, using Eq. (7), one obtains $J = 1.063$. Figure 15 shows the good correlation between the experimental data of [46] and the predicted values obtained from Eq. (6) and values of parameters reported in Table 5.

As it is presented in Fig. 15, the best results are obtained using the optimized model. This is why this model has been adopted for another analysis. This Initiation damage has been implemented into the numerical model and then compared with the experimental data for different strain rates (0.001, 0.01, 0.1 and 0.15 s^{-1}). The results are shown in Fig. 17.

Numerical Analysis of the Aluminum Alloy

In this section, the FE Abaqus software was used to build numerical models and to determine the failure criterion of the Aluminum alloy based tensile and perforation tests. Failure parameters are presented in Table 6, where the values for the tensile test were obtained from experiments while the perforation test values were obtained through numerical analysis and literature data for similar materials [42, 49–51]. It was observed through numerical simulations that the strain

Table 5 Identified parameters of the failure model used for aluminum alloy AW 5005, see Eqs. (6, 7) [36]

Failure model Aluminum alloy (AW 5005)				
$H_1(−)$	$\alpha_1(−)$	$H_2(−)$	$\alpha_2(−)$	$\dot{\varepsilon}_T \; s^{-1}$
0.398	0.63	0.665	− 0.20	1

Table 6 Failure parameters for tension and perforation, [36]. Values reported for tensile tests are experimental data, while numerical modeling has been used to determine values for perforation tests

Test	Tensile test				Perforation test	
	1 (0.001 1/s)	2 (0.01 1/s)	3 (0.1 1/s)	4 (0.15 1/s)	1000 1/s	10,000 1/s
Damage initiation strain $\varepsilon_{D-init}^{pl}$	0.008	0.03	0.08	0.12	0.9	0.96
Displacement at failure (m)u_f	0.0008					
Max. degradation (ratio) (D_{max})	0.6					

It makes possible to reflect a failure mode of the studied material. The damage initiation criterion is expressed using an optimization method, a good correlation over a wide range of strain rates is obtained

$$\varepsilon_{D-init}^{pl} = \begin{cases} f(\dot{\varepsilon}) = H_1 \dot{\varepsilon}^{\alpha_1} & if \, \dot{\varepsilon} \leq \dot{\varepsilon}_T \\ g(\dot{\varepsilon}) = J - H_2 \dot{\varepsilon}^{\alpha_2} & if \, \dot{\varepsilon} \geq \dot{\varepsilon}_T \end{cases} \tag{6}$$

where $\dot{\varepsilon}_T$, J, H_1, α_1, H_2, and α_2 are constant parameters. The parameter $\dot{\varepsilon}_T$ stands for a threshold value, defining a transition between two domains of sensitivities. The plastic strain at damage initiation, $\varepsilon_{D-init}^{pl}$, is continuous such that the following condition holds for the constant J:

rates for perforation tests, $\dot{\varepsilon} = 1000 \; s^{-1}$ and $\dot{\varepsilon} = 10,000 \; s^{-1}$, correspond to initial impact velocities of $V_0 =120$ m/s and $V_0 =180$ m/s, respectively.

Numerical simulations using the FE Abaqus code were conducted to investigate the failure behavior of the Aluminum alloy under different strain rates, ranging from quasi-static to dynamic conditions with impact velocities up to 180 m/s. The shell element type S4R, with 8 degrees of freedom and 4 nodes, and reduced integration [52], was employed for the simulations. The same element type, with an element size of 0.5×0.5 mm, was used for both tension and perforation analyses, as shown in Fig. 16a, and

has been previously demonstrated to be effective for this type of analysis [53–55]. The objective of this numerical analysis was to reproduce the observed failure mode in the experimental tests and identify the constitutive parameters based on those tests, which are listed in Table 5.

The initiation damage law, see Eq. (6) and Fig. 15, has been implemented into the numerical model and compared with the experimental tensile test data for different strain rates (0.001, 0.01, 0.1 and 0.15 s^{-1}). The results are shown in Fig. 17.

The correlation between experimental and numerical results can be observed in Fig. 17. The numerical model exhibited more ductile behavior at the beginning of failure in test 3, while in test 4, it demonstrated ductility at the end stage of failure.

A convergence method was used during perforation test to achieve optimal mesh density and stability of results independent of the mesh size. The mesh was denser in the contact area between the projectile and the 1.0 mm-thick plate, with impact velocities ranging from 40 to 180 m/s as in the experiment. The resulting model consisted of 6048 elements in the central impact zone and 6161 elements of 0.5×0.5 mm size, as illustrated in Fig. 18. Ballistic curves were generated and compared to experimental results in the following section, with the model allowing to predict crack propagation initiation in the internal zone. The
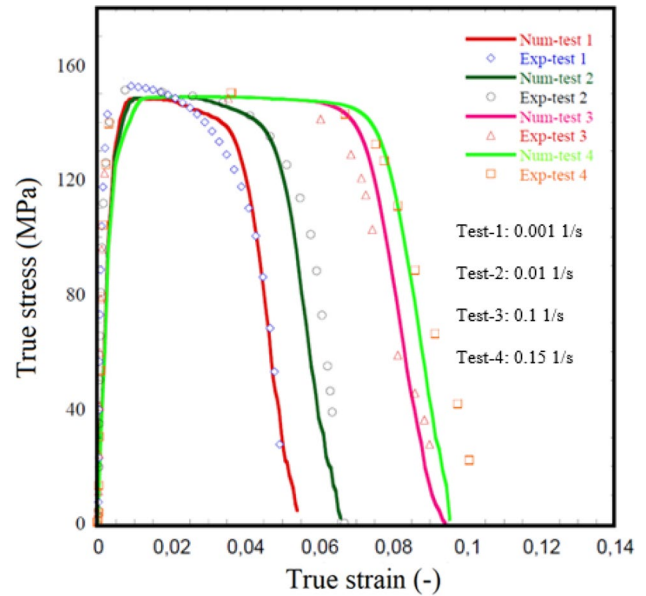
Fig. 17 Comparison between experimental and numerical curves using the optimized initiation damage model [36]

projectile was assumed as rigid to prevent plastic deformation, with a friction coefficient equal to $\mu = 0.2$ [36].

By varying the failure strain level, it was observed that the number of petals decreased for a projectile nose angle
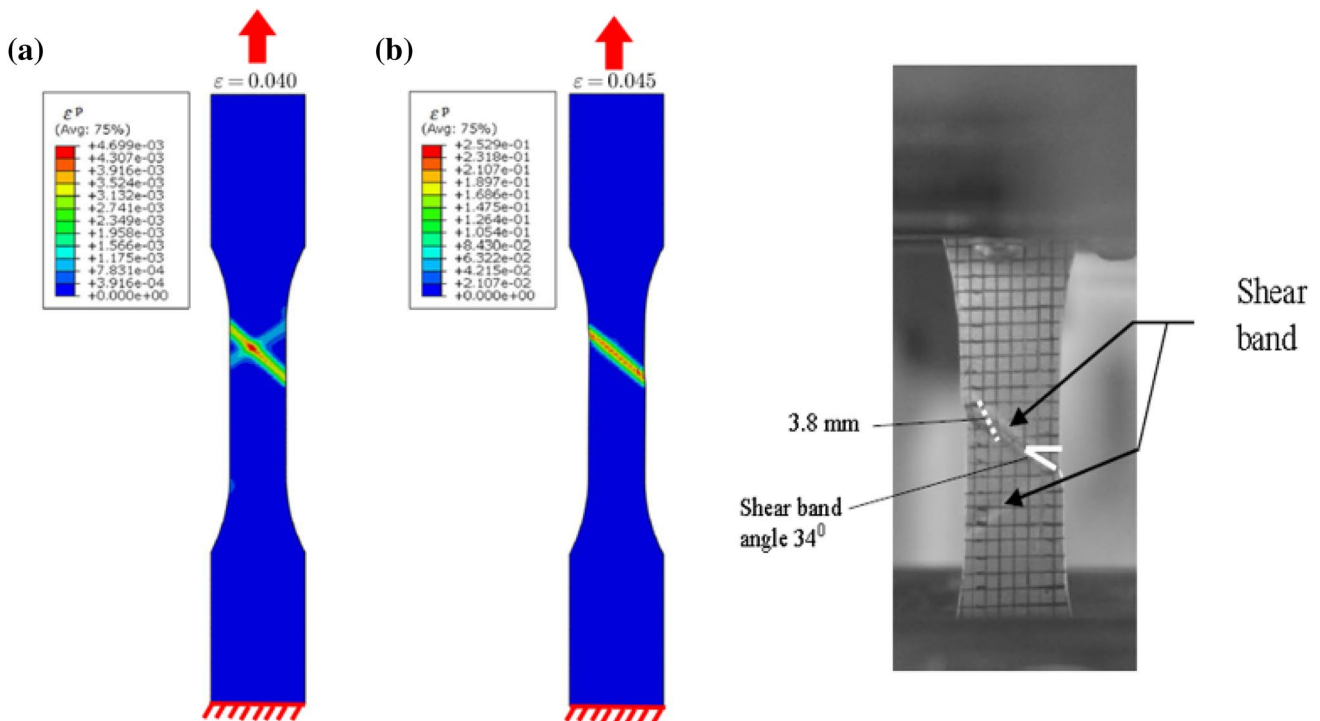

Fig. 16 Numerical simulation of tensile test, **a** equivalent plastic strain distribution for a macroscopic strain equal to $\varepsilon = 0.04$, **b** equivalent plastic strain distribution for macroscopic strain $\varepsilon = 0.045$ [36]
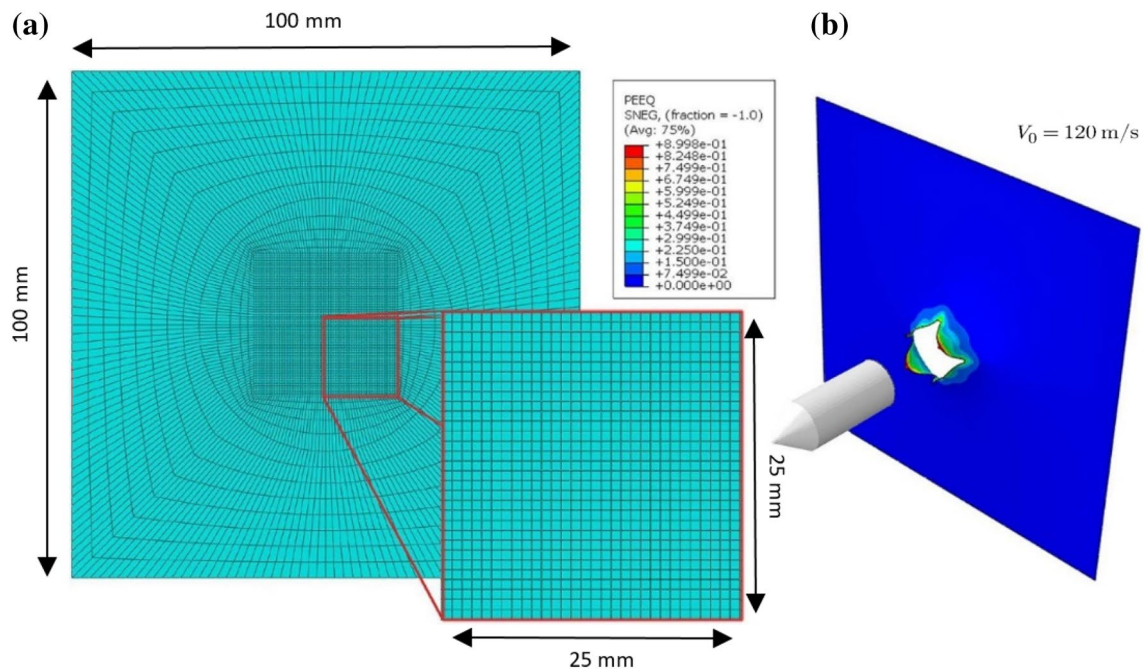
Fig. 18 Numerical model used during numerical simulations and mesh density distribution, **a** mesh, **b** equivalent plastic strain distribution for macroscopic strain [36]

of 72°. An analytical model proposed by [47] for predicting the number of petals was validated through finite element simulations. The Initiation Damage [36] was incorporated into the numerical model and its predictions were compared to experimental data for impact velocities ranging from 40 to 180 m/s. The results are presented in Fig. 20, showing a good agreement between numerical and experimental results. Specifically, Fig. 19 shows that both experimental and numerical models predicted are in agreement with four petals.

Figure 20 displays the experimental and numerical simulation results for a large range of velocities, with a good correlation. The damage initiation criterion [36], Fig. 15 was used to verify the accuracy of the numerical predictions,

confirming the credibility of the failure criterion model. Remarkably, for thicker plates with a thickness of 1.5 mm, the ballistic limit value shifted from 40 m/s to 50 m/s [36].

LDPE Characterization Results

This section focuses on the new results obtained for the static and dynamic behavior of LDPE.

Experimental Results

In this section, experimental tests conducted to identify the mechanical behavior of the polyethylene low density and its influence on the Alucobond structure are presented.

Fig. 19 Numerical result for conical projectile shape, V_0 =120 m/s, comparison between experiments and simulations [36]
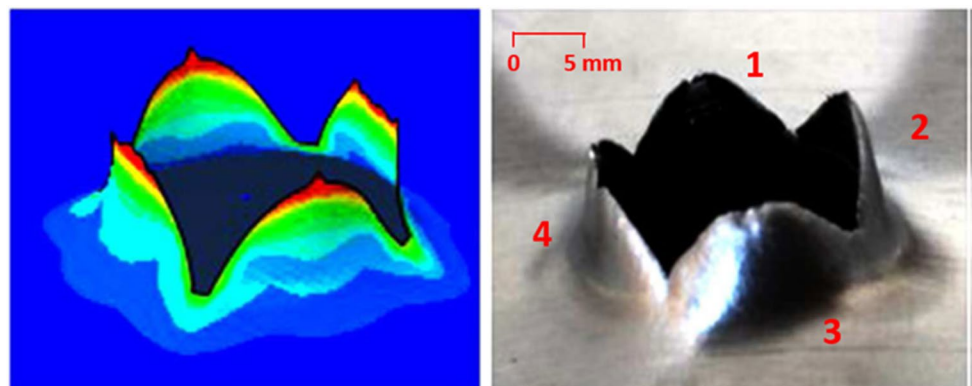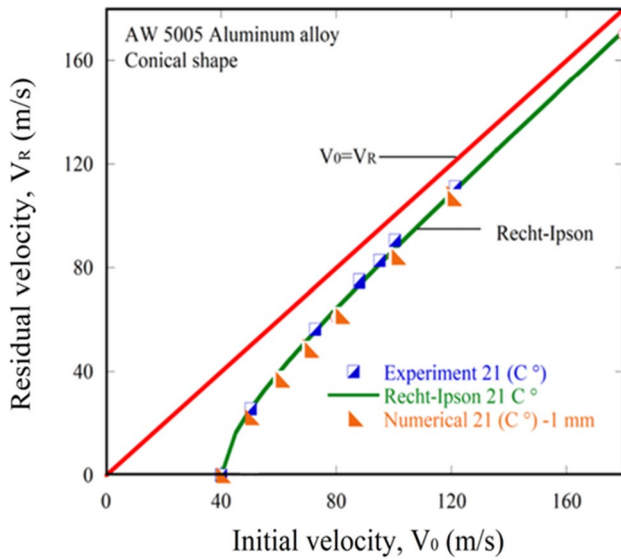
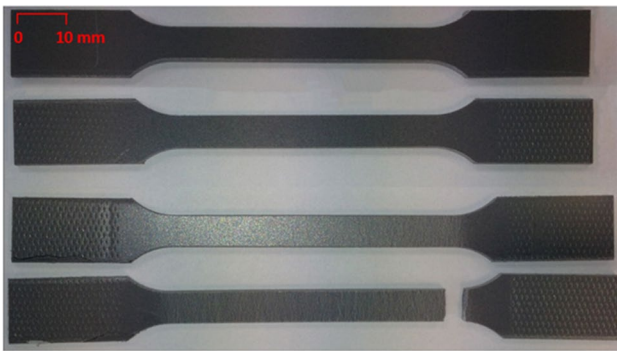**Fig. 20** The ballistic curve in experiment and in simulation [36]

Fig. 21 PE specimen's used during tensile test at different strain rates

Quasi-static tensile and compression tests, at various stain rates in the range (0.0001/s, 0.041/s) were performed.

Compression tests were conducted on cylinders (diameter 10 mm, thickness 4 mm) while tensile tests (Fig. 21) were performed on sample with the dimensions reported in Fig. 7. Figure 22, showing true stress/true strain curves, clearly reveals that the material is highly strain rate sensitive in tension. A positive strain rate sensitivity was observed, the mechanical properties increasing with the strain rate.

The LDPE seems to be more resistant under tensile loading comparing to compression. The LDPE yield stress is about 16.47 MPa at 0.01/s in tension while it is 10.9 MPa in compression at 0.01/s. Moreover, LDPE exposes a remarkable strain hardening in compression comparing to LDPE plastic behavior under tension. As shown in Fig. 22b the compaction zone starts after 60% of strain. During the compression test, a load is applied to the specimen, typically in a gradual and controlled manner. As the load is increased,

the material in the compaction zone undergoes compression, causing it to compact and potentially change in density or volume.

In compression the flow stress increases from 12.45 MPa at 20% deformation to 22.6 MPa at 60% deformation, giving a rise of almost 81.6% in the flow stress. On the other hand, LDPE mechanical behavior appears to be less strain-rate dependent under both tension and compression. In fact, under tensile loading, the yield stress increases from 13.7 MPa at a strain rate of 0.0001/s to 17.2 at 0.041/s and in compression from 10.9 MPa at 0.01/s to 12.19 MPa at 0.1/s.

LDPE Numerical Simulation Analysis

Simulations were performed using explicit numerical Abaqus code with the aim to reproduce experimental results in terms of observed failure modes and to better understand the local response. The numerical simulations were performed at different strain rates under quasi-static loading. The 3D element type is C3D8R: an 8-node linear brick, with reduced integration and hourglass control [52]. This model contains 15,308 nodes and 10,917 elements, element size is (0.5×0.5 mm). The results in terms of force vs displacement are presented in Fig. 24.

In order to describe the yield behavior of the polyethylene, the true stress–strain curves at 0.0001 s^{-1} were introduced into Abaqus directly to predict the elastoplastic behavior, and a Cowper-Symonds model was used to incorporate the strain rate effect.

The Cowper–Symonds material model [56] is a simple elastoplastic, strain hardening, strain rate hardening model that uses the empirical formulation described by Ludwik [57], in which materials are reinforced when plastic deformations are applied. This constitutive relation is known as strain hardening. The Cowper-Symonds model can be written as:

$$\dot{\varepsilon}_{pl} = D(R - 1)^p \tag{8}$$

where D and p are material parameters to be determined from experimental observations, and $\dot{\varepsilon}_{pl}$ is the plastic strain rate. R is the ratio of the yield stress at any strain rate to the static yield stress. Cowper–Symonds assumes that the yield stress σ_s at a high strain-rate has a power-law relationship to the static yield stress σ_0:

$$\sigma_s = \sigma_0 \left[1 + \left(\frac{\dot{\varepsilon}_{pl}}{D} \right)^{\frac{1}{p}} \right] \tag{9}$$

The static yield stress σ_0 was taken equal to 14 MPa, corresponding to the value measured during a tensile test at a reference strain rate of 0.0001 s^{-1}. Figure 23 shows the good agreement between the Cowper–Symonds model
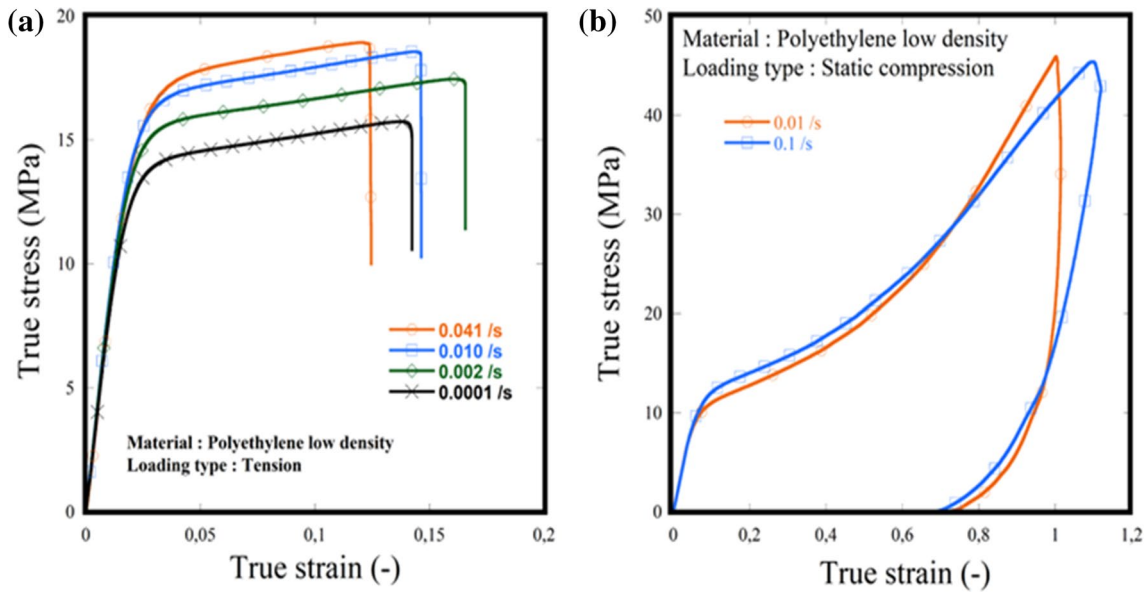
Fig. 22 Stress–strain curves for different strain rates at room temperature, LDPE **a** Tensile test, **b** Compression test
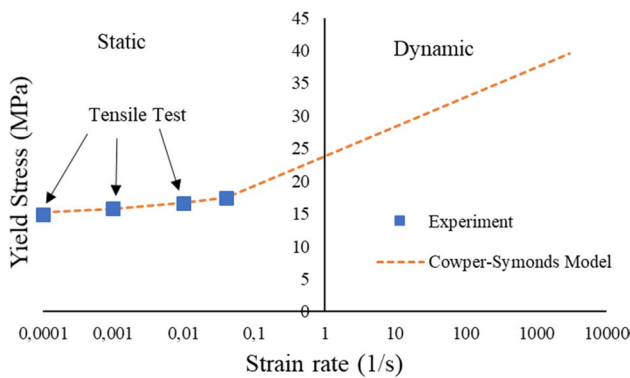

Fig. 23 Experimental data and fitted Cowper–Symonds model showing the relationship between yield stress and strain rate of LDPE

Table 7 LDPE material properties [58]

Tensile strength (MPa)	Density (g/cm3)	Tensile modulus (GPa)	Poisson's ratio (~)
14	0.93	0.25	0.36

Table 8 Coefficients for Cowper–Symonds model of Eq. 8

Material	D (~)	P (~)
LDPE	104	5.61

Table 9 Failure parameters for tension test LDPE material

Test	Tensile test			
	1 (0.0001 1/s)	2 (0.002 1/s)	3 (0.01 1/s)	4 (0.04 1/s)
Displacement at failure (m)u_f	0.012	0.014	0.011	0.010
Max. degradation (ratio) (D_{max})	0.1			

(Eq. 9) compared to experimental data The non-dimensional coefficients D and p for LDPE material are presented in Table 8.

Based on the previously cited parameters (Table 7, 8, 9) numerical simulations were done to predict tensile test at different strain rates. As it might be seen in Fig. 24, there is a good correlation between experimental and numerical results. The response of polyethylene low density (LDPE) was investigated over a wide range of strain rates. The mechanical behavior was found to be strain rate dependent, showing an increase in stress with increasing the initial strain rate.

Characterization Test Results for Alucobond Structure

Experimental Analysis of the Alucobond Structure

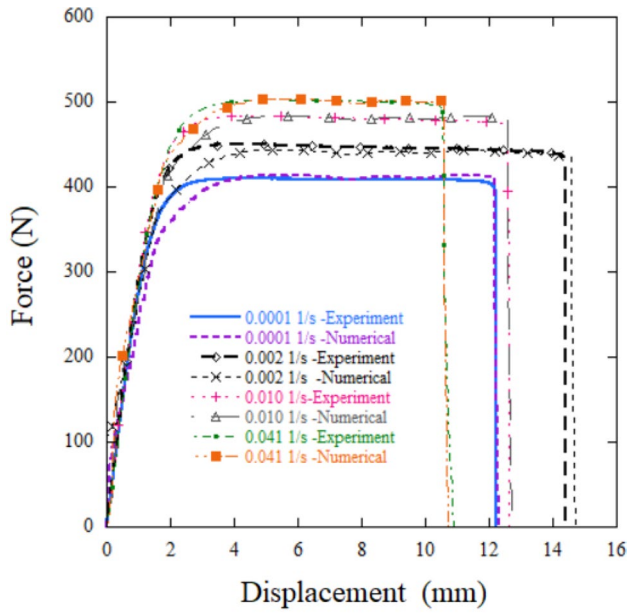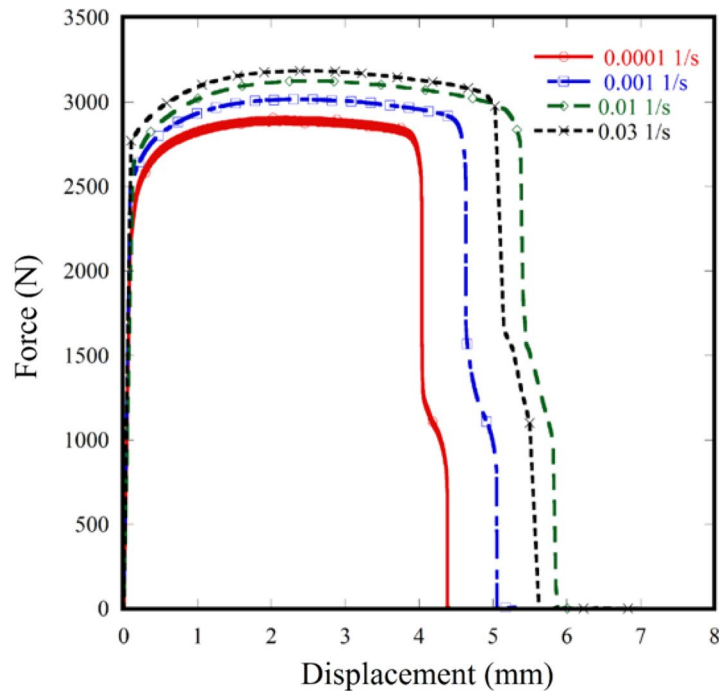The Alucobond sheets of 4 mm (2 layers of 0.5 mm

Fig. 24 Comparison between experimental and numerical curves using LDPE material

Aluminum alloy thickness and 3 mm LDPE sheet thickness, see Fig. 6) were used to produce tensile test specimens and to machine perforation specimen plates, see Figs. 7 and 8. Tensile test experiments are first presented, followed by perforation tests.

Tensile Test of Alucobond Structure

The quasi-static tensile tests were performed for four different strain rates, i.e. 0.0001, 0.001, 0.01 and 0.03 s^{-1}. The quasi-static uniaxial tensile tests of Alucobond were performed using a conventional hydraulic machine. The dimensions of the flat dumbbell-shaped specimen are shown in Fig. 7 [41]. The first part of the specimen is embedded in 40 mm length while the other end of the specimen is fixed to the moving crosshead. The loading force and displacement are recorded during the tests for an imposed crosshead speed V_0. The results of force vs displacement are presented in Fig. 25

It is clearly shown that the composite material is strain rate sensitive. The maximum force reached at a strain rate of 0.0001 s^{-1} is 2650 N while it is increased to 3330 N at 0.03 s^{-1} Since the strain rate dependence of aluminum is negligible (see Sect. "Aluminum alloy AW 5005 characterization results"), it can be deduced that the strain rate sensitivity of the composite material is attributed only to the polymer.

According to these results, an analysis has been done to predict the percentage of supported force by each material. Using Eq. (1) and the thickness of each Alucobond layer. It has been deduced that the AW5005 Aluminum alloy carried 83% of force during the test performed at 0.0001 s^{-1} as summarized in Table 9. By using Eq. (1) along with the thickness of individual Alucobond layers, it has been determined that the AW5005 Aluminum alloy sustained 83% of

Fig. 25 Force vs displacement for different strain rates at room temperature using Alucobond structure

the load during the test conducted at 0.0001 s^{-1}, as outlined in Table 10.

Perforation Test of Alucobond Structure

This part describes the mechanical behavior of Alucobond structure under impact loading at room temperature and 100 °C. Experimental, analytical and numerical investigations have been carried out to analyze the perforation process [42]. A wide range of impact velocities from 40 to 180 m/s at temperatures ranging from room temperature to 100 °C has been covered during the tests. A conical projectile with an angle of 72° has 13 mm in diameter and the specimen is 4 mm thick. The active part of the specimen during perforation is presented in Fig. 7. The results obtained at room temperature, in terms of the ballistic curve V_R-V_0 and the absorbed energy are reported in Fig. 26.

The residual velocity of the projectile can be calculated using Eq. 3 with $V_B = 63 m/s$, and the ballistic curve shape parameter $\kappa = 1.82$. The absorbed energy by the plate E_d can be calculated using Eq. 4. The minimum energy required to perforate the plate is 52 J ($m_P = 28g$ and $V_0 = V_B = 63 m/s$).

Figure 27 shows the failure pattern for an initial impact velocity of $V_0 = 71.63$ m/s, resulting in a residual velocity of V_R=34.89 m/s. Four petals are observed. The same failure pattern is observed at $V_0 = 125.3$ m/s with V_R=104.60 m/s, and the number of petals remains constant for impact velocities ranging from 40 to 180 m/s. A more detailed discussion of the number of petals and failure modes for different projectile shapes can be found in [47]. To achieve perforation tests at high impact velocity and high temperature, a pneumatic gas gun equipped with the thermal chamber detailed in Sect. "Perforation test using a thermal chamber" has been used.

Figure 28 shows a comparison of experimental results at room temperature, 60 and 100 °C. It can be observed that increasing the initial temperature of the specimen reduces the ballistic limit (non-perforation state) to lower values: the obtained ballistic limit using the conical projectile is approximately 60 m/s for T = 21 °C, 42 m/s for T = 60 °C and 40 m/s for T = 100 °C. Whereas the shape parameter K is 1.82 for T = 21 °C, 2.0 for T = 60 °C, and 2.3 for T = 100 °C respectively. For elevated temperatures, the other measured values are shifted when higher residual velocities V_R are measured. The energy absorbed during the impact does not change considerably with the value of impact Figs 29, 30 velocity, as reflected in.

Experimental results stay in accordance with analytical predictions using Eq. 3 [43]. The plastic deformation energy dissipated during the perforation process is transformed into thermal energy and induces a considerable increase of temperature in petals.

As a result, the observed failure modes depends on both impact velocity and initial temperature values. The conical
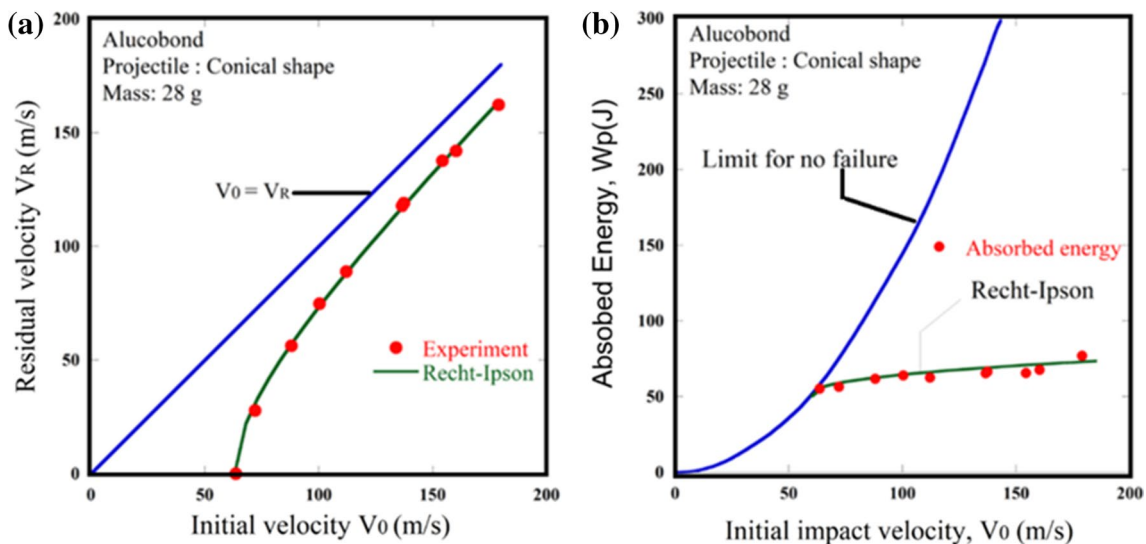
Table 10 Calculated force during the tensile test performed at 0.0001 s^{-1}

Material	Calculated force (N)
LDPE	450
Aluminum alloy AW5005	2205
Total force	2655

Fig. 26 **a** Ballistic curve obtained during perforation and determination of the ballistic limit, **b** Energy absorbed by the plate during impact test, determination of the failure energy (room temperature)

Fig. 27 Experimental observation of failure patterns, $V_0 =$ 71.63 m/s and 125.3 m/s
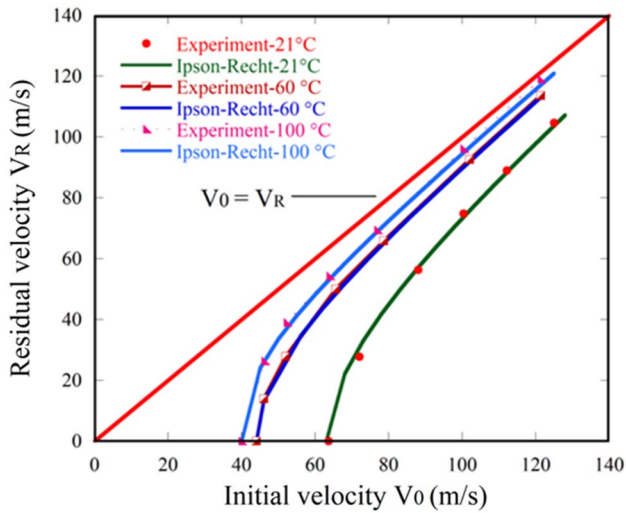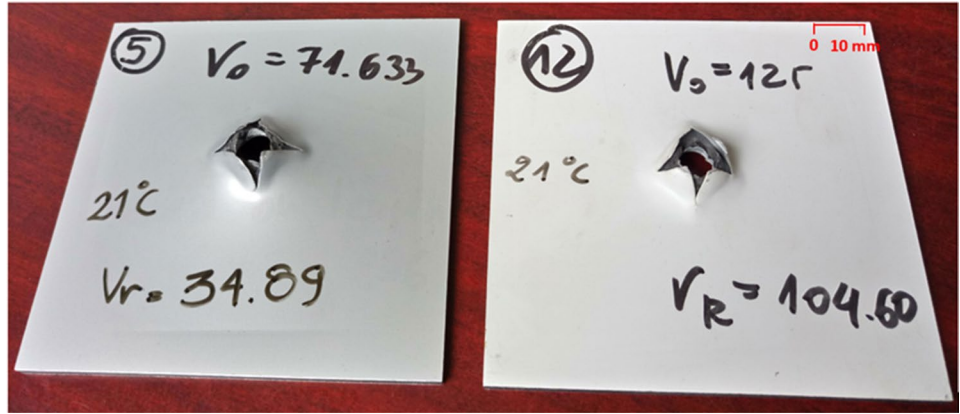

Fig. 28 Alucobond structure, Impact velocity V_0 vs residual velocity V_R—experimental results for T = 21°C, T = 60°C and T = 100°C; using conical projectiles
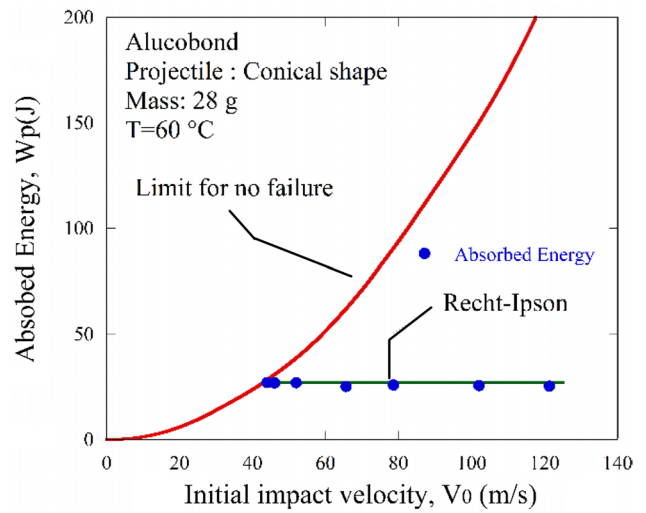

Fig. 29 Energy absorbed by the plate during impact test at 60° C, determination of the failure energy

projectile perforates the target plate and the plastic strain is localized at the extremities of the petals. The number of petals strongly depends on the failure deformation parameter. This parameter changes with temperature and the projectile shape. In this study, five petals are observed for temperatures over 100 °C, whereas three or four petals usually appear at lower temperatures.

The formation of four petals is the usual failure mode. Up to five petals were observed at higher impact velocities and temperatures. The failure modes observed during experiments are presented in Fig. 31

Modeling and Numerical Simulation

Tensile Test of Alucobond Structure

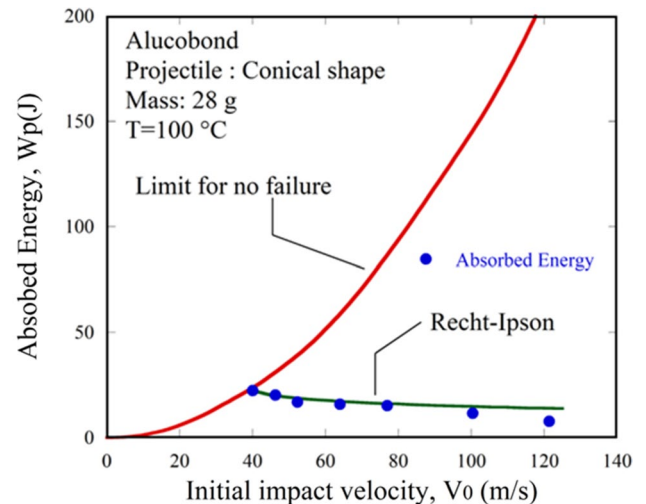In order to perform the experimental results, numerical simulations were done for tensile and perforation test on

Fig. 30 Energy absorbed by the plate during impact test at 100° C, determination of the failure energy

Fig. 31 Initial temperature effect and impact velocity during perforation. Experimental observations of petaling failure mode, **a** 4 petals at T = 60°C and V_0 = 78,62 m/s, **b** 5 petals at T = 100 °C and V_0 = 93,94 m/s
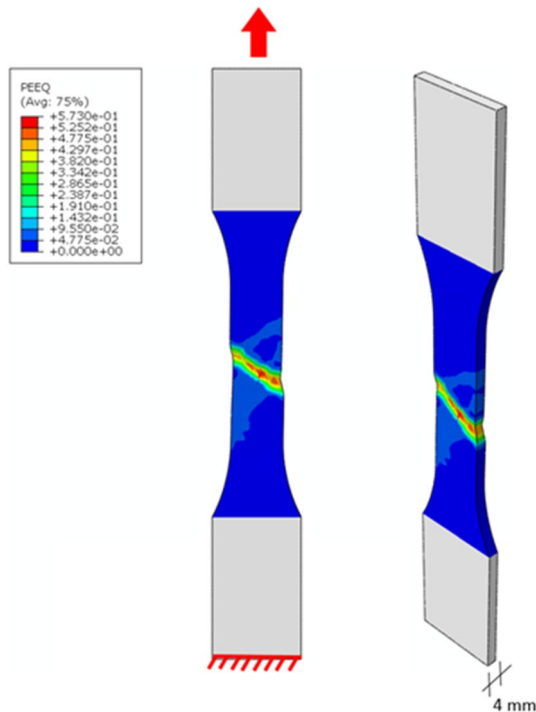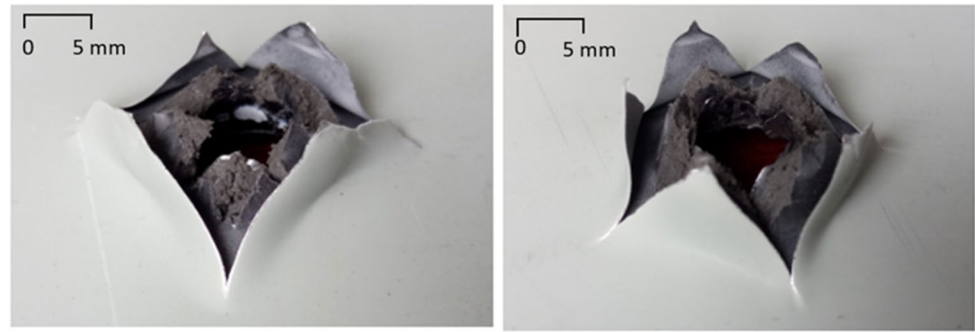

Fig. 32 Numerical simulation of tensile test (Alucobond)

Alucobond. Shell element S4R with 24 degrees of freedom and 4 nodes were used. The number of elements was 16,356 to model the Aluminium alloy layers (Fig. 32).

In the other hand the polyethylene part was modelled using 3D element types C3D8R [52]. This model contains 15,308 nodes and 10,917 elements; element size is (0.5 × 0.5 mm). The results in terms of force vs displacement are presented in Fig. 33.

As it might be seen in the Fig. 33, there is a good correlation between experimental and numerical results. The response of ALUCOBOND was investigated at quasi-static range of strain rates. The mechanical behavior was found to be strain rate dependent.

Perforation Test

As previously, shell elements (S4R) were used for the aluminum layer and solid elements (C3D8R) for polyethylene layers. The mesh is denser along the projectile-plate contact zone where the thickness of the single aluminum plate in this area is 0.5 mm. The initial projectile velocity is defined in the predefined fields with impact velocities ranging from 40 to 180 m/s as conceded in the experiment. This model contains 6048 elements in the central part of impact, and 6161 using the same element size (0.5 × 0.5 mm). The suggested finite element model used for the LDPE plate with 3 mm of thickness is intended for a 3D analysis of the impact and perforation problem, in order to take into account, the influence of the thickness. The projectile was modelled as a three-dimensional non-deformable rigid body with a reference point to affect mass, velocity and moment of inertia. The contact between the projectile and the plate was modelled using the penalization method with a reduced slip formulation. A constant coefficient of friction μ = 0.2 was applied based on the experimental studies. In order to optimize the mesh, taking into account the element type, mesh density and the computation time, the chosen method, after having tried several approaches, was to partition the geometry of the plate in two parts: a square part of 28 × 28 mm (784 mm^3) and an outer part that completes the parallelepiped structure of 100 × 100 × 3 mm^3 dimensions (LDPE part), Fig 34.

The square part of the plate was meshed using C3D8R elements. For a plate thicknesses of 0.5 and 3 mm, using the hexahedral linear elements of initial size $\Delta_x = \Delta_z = \Delta_z = 0.2$ mm in the impact zone makes it possible to ensure the stability of the digital solution without the influence of the mesh density with an optimal computation time. Therefore, the central part of our numerical model for the 3 mm plate contains 135,270 finite elements (3 elements in thickness). The outer part of the plate has been meshed using hexahedral elements C3D8I (incompatible 8-node linear elements [52]). These elements have an additional degree of freedom that improves the ability to model a displacement gradient across the element, these elements act as quadratic elements. The use of incompatible mode elements produces results
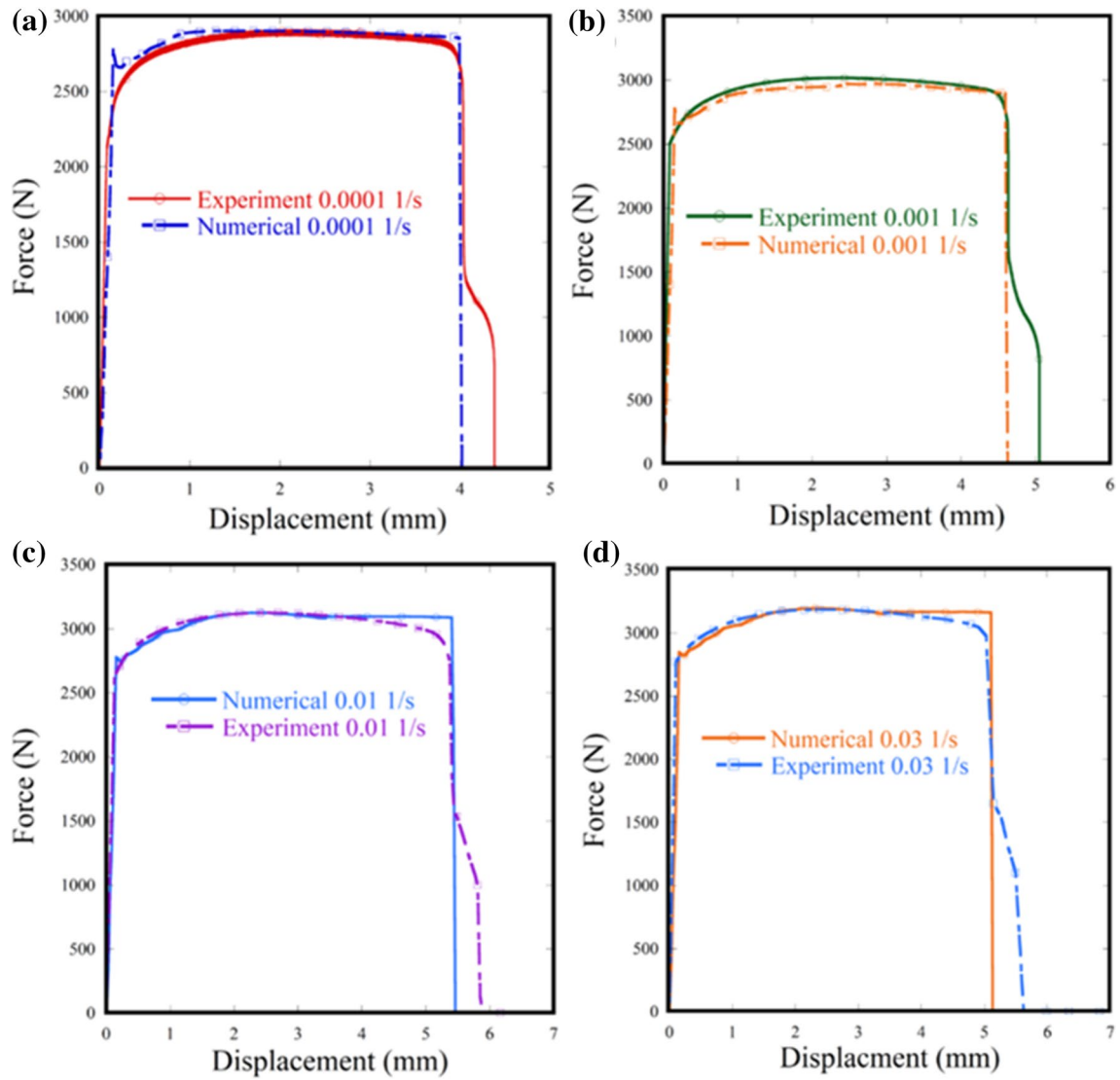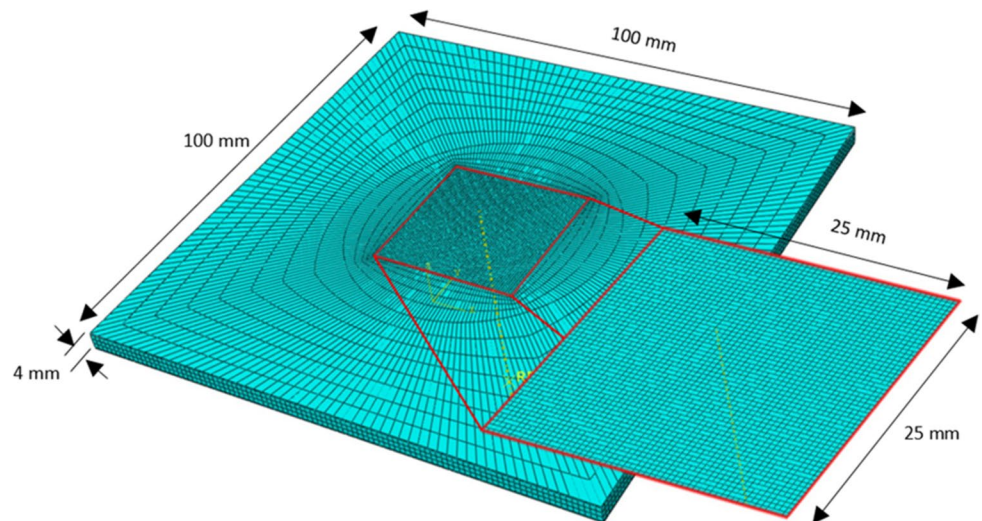
Fig. 33 Comparison between experimental and numerical curves using Alucobond structure

Fig. 34 Numerical model used
during numerical simulations
and mesh density distribution

comparable to quadratic elements with a lower computation time. The result of these numerical simulations are presented in Fig. 35.

After modeling the perforation and tensile tests with different parameters, and comparing the numerical results with the experimental data, good correlations were found between both results as shown in Fig. 35a–c. this confirms that both the chosen model and parameters are correct.

As it is shown in Fig. 36, the number of petals is the same as in the experiments, four petals are observed. It was reported that the number of petals N observed during dynamic perforation using a conical projectile shape, was related to the nose angle. In this work, one angle (72°) has been used to analyze the results.

This testing approach, which uses a thermal chamber for impact loading, allows the verification of the material's behavior, interesting results were obtained for Alucobond heated to elevated temperatures. The failure mode in form of petals confirmed analytical and numerical considerations in which the petals number varied from 3 to 5. The studies on initial impact velocity and residual impact velocities reproduced typical behavior of the structure. The energy absorbed during perforation is quasi-constant for the studied range of velocities (up to 123 m/s). Using conical shaped projectile, the average value was 52 J at room temperature and decreased to an average of 17 J at 100 °C. The measured ballistic limit for the conical shaped projectile is equal to 61 m/s at room temperature and diminished to 41 m/s at 100 °C.

Conclusion

The primary focus of this work is to investigate the impact behavior of a sandwich structure called Alucobond, which comprises two dissimilar materials: AW5005 aluminum alloy and LDPE low-density polyethylene. The research approach involves conducting a comprehensive study of each material separately, followed by a thorough examination of the tested structure, based on two modes of characterization: quasi-static and dynamic. Quasi-static tests consist of tensile tests with a different strain rates of 0.0001, 0.001, 0.01 and 0.03 s^{-1}, whereas dynamic tests consist of perforation test (impact loading) at a strain rate margin between $10^{-4}\ s^{-1} \leq \dot{\varepsilon} \leq 10^{4}\ s^{-1}$ with varying temperatures from 21 to 300 °C.

The two instruments used in dynamic tests are new in the experimental field and are the subject of other scientific publications. More technical and experimental details were presented.

The dynamic impact behavior of the two materials was analyzed during this study by means of experimental tests. These tests gave rise to analytical modeling and numerical simulations in order to obtain a more precise description via local measurements.
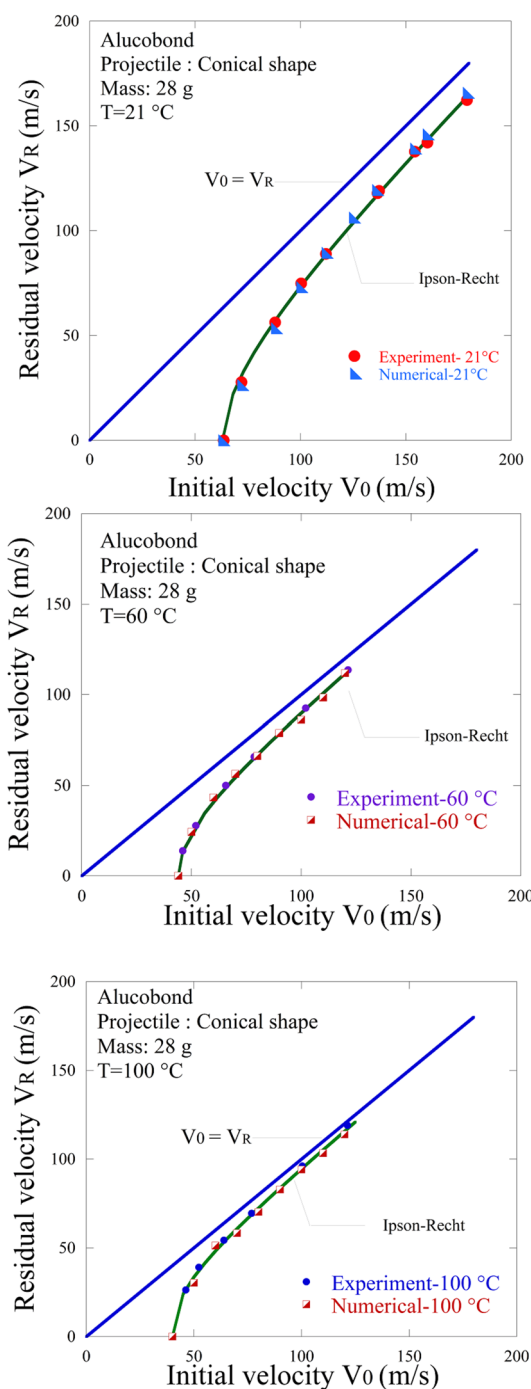

Fig. 35 Comparison of the ballistic curves between experiments and simulations for different temperatures 21, 60 and 100 °C

Analyzing the experimental results for both materials: Aluminum AW5005 and LDPE low density polyethylene, showed that these two materials are completely different, one of them is not sensitive to strain rate which is the aluminum AW5005, and the other one, the LDPE is very strain rate sensitive. It has been shown that in the range of strain rates between ($10^{-4}\ s^{-1} \leq \dot{\varepsilon} \leq 10^{-3}\ s^{-1}$) the deformation

Fig. 36 The comparison of the failure patterns between experiments and simulations (for conical projectile shape, V_0 = 120 m/s)
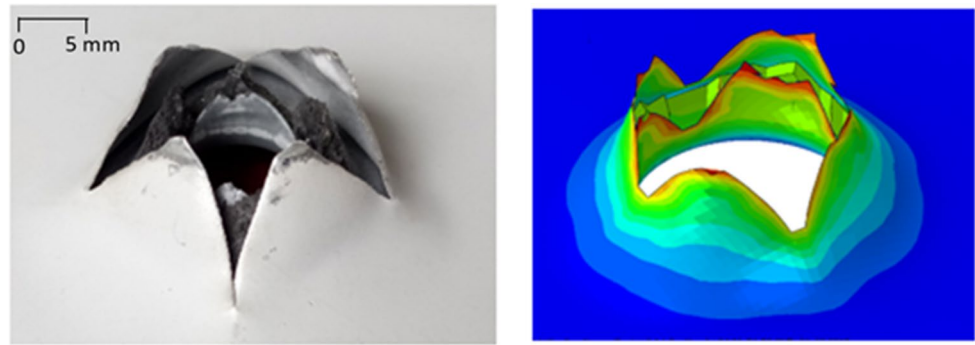
mechanisms involved in both materials are thermally activated.

The dynamic aging phenomenon results in a decrease of the flow stress for aluminum in a given velocity and temperature range (293 K ≤ T ≤ 443 K).

Preliminary analyzes of the Alucobond structure, specifically in quasi-static, have shown that it is very strain-rate sensitive as illustrated in Fig. 27. It can be deduced that Aluminum alloy supports 83% of the force during the test, however the low-density polyethylene supports 17% of the force.

Same observations have been made for perforation at high temperatures, the structure becomes soft (temperature-sensitive), the limit of ballistic velocity decreases with temperature increase as illustrated in Fig. 28.

Experimentally, impact and perforation tests have been performed using a gas gun equipped with two devices for measuring the projectile's velocity (the initial and residual velocity sensors) that were developed specifically for this project. It was thus possible to determine the absorbed energy by the impacted targets through complete energy balance equations. The used projectile during the tests has a mass of m_p=28 g, a mode of rupture by petal formation inducing a radial necking was observed.

Three primary physical mechanisms have been recognized as the primary factors contributing to the energy absorption during the perforation of a metal target. These include the global deflection of the target, elastic deformation, and localized plastic deformation in the impact zone. It is important to acknowledge that there may be other phenomena at play, such as friction between the projectile and the structure.

The mechanical response of aluminum and Alucobond structures under impact and perforation has been simulated through a 3D finite element (FE) model using the Abaqus/Explicit FE software. The Johnson–Cook constitutive model for aluminum and Cowper Symonds model for LDPE were implemented in the code to describe the material behavior. Failure criterion modes have been developed for the used materials. It has been noted that

while the low-density polyethylene is sensitive to both strain rate and temperature, the Aluminum alloy AW5005, in contrast, is not sensitive to strain rate but is temperature-sensitive. The identification of the parameters of the two constitutive relations was possible by means of analytical modeling of the experimental results from the characterization tests.

This sandwich beams structure can be used in order to increase the stiffness / mass ratio of structures in civil and mechanical engineering, aerospace and automotive. It can be used as energy absorbers in case of impact due to their plastic deformation dissipated at an almost constant level of effort over a wide range of deformations. An example is the crash-box used to absorb kinetic energy in the event of a collision of a vehicle. However, it can be used for damping vibrations in machine tools and fire resistance in buildings. Alucobond is also an excellent acoustic and thermal insulator when used as a closed cell structure, it also has an excellent heat transfer and chemical exchange capacity as demonstrated in this work. For example, in Japan, foams such as Alporas foam are used as an acoustic isolator along highways to reduce noise, and in the railway tunnel to mitigate sonic shock waves. In aircraft industry, Alucobond structures can be used to reduce the noise that is generated by the engine's turbine. Some multi-functional applications are naturally difficult to implement, but often it would be possible to satisfy a dual interest application, for example Queryweight reduction and sound isolation.

Declarations

References

1. Gibson LJ, Ashby MF (1997) Cellular solids: structure and properties, 2nd edn. Cambridge University Press, Cambridge
2. Hollaway LC (ed) (1994) Handbook of polymer composites for engineers. Woodhead publishing, Sawston
3. Xie W, Yang F, Meng S, Scarpa F, Wang L (2020) Perforation of needle-punched carbon-carbon composites during high-temperature and high-velocity ballistic impacts. Compos Struct 245:112224
4. Sharif U, Sun B, Hussain S, Ibrahim DS, Adewale OO, Ashraf S, Bashir F (2021) Dynamic behavior of sandwich structures with magnetorheological elastomer: a review. Materials 14(22):7025
5. Topkaya T, Solmaz MY (2018) Investigation of low velocity impact behaviors of honeycomb sandwich composites. J Mech Sci Technol 32:3161–3167
6. Selvaraj R, Maneengam A, Sathiyamoorthy M (2022) Characterization of mechanical and dynamic properties of natural fiber reinforced laminated composite multiple-core sandwich plates. Compos Struct 284:115141
7. Bendarma A, Gourgue H, Jankowiak T, Rusinek A, Kardellass S, Klosak M (2020) Perforation tests of composite structure specimens at wide range of temperatures and strain rates-experimental analysis. Mater Today: Proc 24:7–10
8. Bauwens JC (1972) Relation between the compression yield stress and the mechanical loss peak of bisphenol-A-polycarbonate in the β transition range. J Mater Sci 7:577–584
9. Argon AS (1973) A theory for the low-temperature plastic deformation of glassy polymers. Phil Mag 28(4):839–865
10. Ward IM, Sweeney J (2012) Mechanical properties of solid polymers. Wiley, Hoboken
11. G'sell C, Gopez AJ (1985) Plastic banding in glassy polycarbonate under plane simple shear. J Mater Sci 20:3462–3478
12. G'Sell C, Hiver JM, Dahoun A, Souahi A (1992) Video-controlled tensile testing of polymers and metals beyond the necking point. J Mater Sci 27:5031–5039
13. G'sell, C. (1995). Introduction à la mécanique des polymères, Chapitre loi de comportement mécanique des polymères solides. G'sell-Haudin, Ed. INPL-MECAMAT-GFP-APPLOR-FIRTECH.
14. Garcia-Gonzalez D, Rusinek A, Bendarma A, Bernier R, Klosak M, Bahi S (2020) Material and structural behaviour of PMMA from low temperatures to over the glass transition: quasi-static and dynamic loading. Polym Test 81:106263
15. Arruda EM, Boyce MC, Jayachandran R (1995) Effects of strain rate, temperature and thermomechanical coupling on the finite strain deformation of glassy polymers. Mech Mater 19(2–3):193–212
16. Jordan JL, Casem DT, Bradley JM, Dwivedi AK, Brown EN, Jordan CW (2016) Mechanical properties of low density polyethylene. J Dyn Behav Mater 2:411–420
17. Meyers MA (1994) Dynamic behavior of materials. Wiley, Hoboken
18. Fan Z, Fang X, Ji S (2005) Microstructure and mechanical properties of rheo-diecast (RDC) aluminium alloys. Mater Sci Eng A 412(1–2):298–306
19. Wu HC, Yip MC (1980) Strain rate and strain rate history effects on the dynamic behavior of metallic materials. Int J Solids Struct 16(6):515–536
20. Field JE, Walley TM, Proud WG, Goldrein HT, Siviour CR (2004) Review of experimental techniques for high rate deformation and shock studies. Int J Impact Eng 30(7):725–775
21. Yadav S, Chichili DR, Ramesh KT (1995) The mechanical response of a 6061–T6 A1/A12O3 metal matrix composite at high rates of deformation. Acta Metall Mater 43(12):4453–4464
22. Lambert, J. P., & Jonas, G. H. (1976). Towards standardization in terminal ballistics testing: velocity representation. Army ballistic research lab aberdeen proving ground MD.
23. Garouge SE, Tarfaoui M, Hassoon OH, Minor HE, Bendarma A (2022) Effect of stacking sequence on the mechanical performance of the composite structure under slamming impact. Mater Today: Proc 52:29–39
24. Jankowiak T, Rusinek A, Bendarma A (2018) Protocol to define material behaviour and failure strain level at low and high strain rates based on compression test. J Theor Appl Mech 56(2):471–481
25. Bendarma A, Jankowiak T, Rusinek A, Lodygowski T, Klosak M (2019) Perforation tests of aluminum alloy specimens for a wide range of temperatures using high-performance thermal chamber-experimental and numerical analysis. IOP Conf Ser: Mater Sci Eng 491(1):012027
26. Jia B, Rusinek A, Bahi S, Bernier R, Pesci R, Bendarma A (2019) Perforation behavior of 304 stainless steel plates at various temperatures. J Dyn Behav Mater 5:416–431
27. Akhzouz H, El Minor H, Tatane M, Bendarma A (2021) Physical characterization of bio-composite CEB stabilized with Argan nut shell and cement. Mater Today: Proc 36:107–114
28. Bendarma A, Rusinek A, Jankowiak T, Lodygowski T, Jia B (2021) Experimental analysis of the aluminum alloy sheet subjected to impact and perforation process. Mater Today: Proc 36:88–93
29. Garouge SE, Tarfaoui M, Minor HE, Bendarma A (2022) The improvement of the physical and mechanical properties of CNTs based composite material. Mater Today: Proc 52:64–70
30. Jia B, Rusinek A, Pesci R, Bernier R, Bahi S, Bendarma A, Wood P (2021) Simple shear behavior and constitutive modeling of 304 stainless steel over a wide range of strain rates and temperatures. Int J Impact Eng 154:103896
31. Bendarma A, Garouge SE, Rusinek A, Akhzouz H, Kardellass S, Bouslikhane S, Minor HE (2022) The behaviour of aluminum alloy 1050 sheet subjected to impact and perforation process: experimental and numerical approaches. Mater Today: Proc 52:40–44
32. Klosak M, Jankowiak T, Rusinek A, Bendarma A, Sielicki PW, Lodygowski T (2020) Mechanical properties of brass under impact and perforation tests for a wide range of temperatures: experimental and numerical approach. Materials 13(24):5821
33. Bendarma A, Jankowiak T, Rusinek A, Lodygowski T, Jia B, Miguélez MH, Klosak M (2020) Dynamic behavior of aluminum alloy Aw 5005 undergoing interfacial friction and specimen configuration in split Hopkinson pressure bar system at high strain rates and temperatures. Materials 13(20):4614
34. ALUCOBOND (2017) https://www.transport-industry.com/fr/alucobond.html
35. Kulekci MK (2014) Effects of process parameters on tensile shear strength of friction stir spot welded aluminium alloy (EN AW 5005). Arch Metall Mater 59:221–224

36. Bendarma A, Jankowiak T, Łodygowski T, Rusinek A, Klósak M (2017) Experimental and numerical analysis of the aluminum alloy AW5005 behavior subjected to tension and perforation under dynamic loading. J Theor Appl Mech 55(4):1219–1233

37. Sen SK, Raut S (2015) Microbial degradation of low density polyethylene (LDPE): a review. J Environ Chem Eng 3(1):462–473

38. Malpass DB (2010) Introduction to industrial polyethylene: properties, catalysts, and processes. Wiley, Hoboken

39. Roy PK, Titus S, Surekha P, Tulsi E, Deshmukh C, Rajagopal C (2008) Degradation of abiotically aged LDPE films containing pro-oxidant by bacterial consortium. Polym Degrad Stab 93(10):1917–1922

40. Instron, s.d. http://www.eurotherm.tm.fr/products/controllers/. [En ligne] http://www.instron.us/en-us/

41. Zhong WZ, Mbarek IA, Rusinek A, Bernier R, Jankowiak T, Sutter G (2016) Development of an experimental set-up for dynamic force measurements during impact and perforation, coupling to numerical simulations. Int J Impact Eng 91:102–115

42. Kpenyigba KM, Jankowiak T, Rusinek A, Pesci R (2013) Influence of projectile shape on dynamic behavior of steel sheet subjected to impact and perforation. Thin-Walled Structures 65:93–104

43. Recht R, Ipson TW (1963) Ballistic perforation dynamics. J Appl Mech. https://doi.org/10.1016/j.tws.2013.01.003

44. Jones N, Paik JK (2012) Impact perforation of aluminium alloy plates. Int J Impact Eng 48:46–53

45. Jones N, Birch RS, Duan R (2008) Low-velocity perforation of mild steel rectangular plates with projectiles having different shaped impact faces. J Press Vessel Technol 10(1115/1):2937767

46. Grytten F, Børvik T, Hopperstad OS, Langseth M (2009) Low velocity perforation of AA5083-H116 aluminium plates. Int J Impact Eng 36(4):597–610

47. Atkins AG, Liu JH (1998) Necking and radial cracking around perforations in thin sheets at normal incidence. Int J Impact Eng 21(7):521–539

48. Johnson, G. R. (1983). A constitutive model and data for materials subjected to large strains, high strain rates, and high temperatures. Proc 7th Inf Sympo Ballistics 541–547.

49. Landkof B, Goldsmith W (1985) Petalling of thin, metallic plates during penetration by cylindro-conical projectiles. Int J Solids Struct 21(3):245–266

50. Jankowiak T, Rusinek A, Wood P (2013) A numerical analysis of the dynamic behaviour of sheet steel perforated by a conical projectile under ballistic conditions. Finite Elem Anal Des 65:39–49

51. Jankowiak T, Rusinek A, Kpenyigba KM, Pesci R (2014) Ballistic behavior of steel sheet subjected to impact and perforation. Steel Compos Struct 16(6):595–609

52. Abaqus, 2014. Abaqus/Explicit User's Manuels, Version 6.14. s.l.:s.n.

53. Ambati M, De Lorenzis L (2016) Phase-field modeling of brittle and ductile fracture in shells with isogeometric NURBS-based solid-shell elements. Comput Methods Appl Mech Eng 312:351–373

54. Amiri F, Millán D, Shen Y, Rabczuk T, Arroyo M (2014) Phase-field modeling of fracture in linear thin shells. Theoret Appl Fract Mech 69:102–109

55. Elnasri I, Zhao H (2016) Impact perforation of sandwich panels with aluminum foam core: a numerical and analytical study. Int J Impact Eng 96:50–60

56. Cowper, G. R., & Symonds, P. S. (1957). Strain-hardening and strain-rate effects in the impact loading of cantilever beams. Brown Univ Providence Ri.

57. Ludwik, P. (1909). Element der technologischen. Mechanik 32.

58. Xu MM, Huang GY, Feng SS, Qin XY, McShane GJ, Stronge WJ (2016) Perforation resistance of aluminum/polyethylene sandwich structure. Mater Des 100:92–101